



Kent Academic Repository

Huang, Yizhi, Hossain, MD Moinul, Cao, Xun, Zhang, Biao, Li, Jian and Xu, Chuanlong (2023) *A simultaneous measurement technique for soot temperature and volume fraction of sooting flames considering self-absorption through hyperspectral imaging*. *Optics and Lasers in Engineering*, 160 . ISSN 0143-8166.

Downloaded from

<https://kar.kent.ac.uk/97001/> The University of Kent's Academic Repository KAR

The version of record is available from

<https://doi.org/10.1016/j.optlaseng.2022.107285>

This document version

Author's Accepted Manuscript

DOI for this version

Licence for this version

CC BY-NC-ND (Attribution-NonCommercial-NoDerivatives)

Additional information

Versions of research works

Versions of Record

If this version is the version of record, it is the same as the published version available on the publisher's web site. Cite as the published version.

Author Accepted Manuscripts

If this document is identified as the Author Accepted Manuscript it is the version after peer review but before type setting, copy editing or publisher branding. Cite as Surname, Initial. (Year) 'Title of article'. To be published in *Title of Journal*, Volume and issue numbers [peer-reviewed accepted version]. Available at: DOI or URL (Accessed: date).

Enquiries

If you have questions about this document contact ResearchSupport@kent.ac.uk. Please include the URL of the record in KAR. If you believe that your, or a third party's rights have been compromised through this document please see our [Take Down policy](https://www.kent.ac.uk/guides/kar-the-kent-academic-repository#policies) (available from <https://www.kent.ac.uk/guides/kar-the-kent-academic-repository#policies>).

Title:

A simultaneous measurement technique for soot temperature and volume fraction of sooting flames considering self-absorption through hyperspectral imaging

The type of article: Full-length Paper

Authors and affiliations:

Yizhi Huang¹, Md Moinul Hossain², Xun Cao³, Biao Zhang¹, Jian Li¹,

Chuanlong Xu^{1, *}

1. Key Laboratory of Energy Thermal Conversion and Control of Ministry of Education, School of Energy and Environment, Southeast University, Nanjing, 210096, China
2. School of Engineering, University of Kent, Canterbury, Kent, CT2 7NT, UK
3. School of Electronic Science and Engineering, Nanjing University, Nanjing, 210093, China

E-mail address:

230189043@seu.edu.cn (Y. Huang)

M.Hossain@kent.ac.uk (M. M. Hossain)

caoxun@nju.edu.cn (X. Cao)

zhangbiao@seu.edu.cn (B. Zhang)

eelijian@seu.edu.cn (J. Li)

chuanlongxu@seu.edu.cn (C. Xu)

*Corresponding author :

Name: Chuanglong Xu

Address: School of Energy and Environment, Southeast University, Nanjing, 210096, China

Tel&Fax: +86-025-83794395

Email address: chuanlongxu@seu.edu.cn

A simultaneous measurement technique for soot temperature and volume fraction of sooting flames considering self-absorption through hyperspectral imaging

Abstract

Due to the complex optical properties of sooting flames, the accuracy of flame emission-based measurement techniques depends on an appropriate self-absorption correction strategy. Thus, this paper presents a novel iterative procedure to retrieve the soot temperature and volume fraction of sooting flames along with a self-absorption correction strategy through hyperspectral imaging. Numerical simulations were carried out on suppositional flames to investigate the performance of the proposed technique. Relative errors obtained from the simulations are below 1.5%, indicating a better accuracy can be achieved by the proposed reconstruction technique. A hybrid camera hyperspectral video imaging technique is designed and implemented with the concept of compressed sensing. A significant improvement in flame spectrum acquisition has been observed. Experiments were carried out under ethylene-air diffusion flames to validate the technique. The reconstructed flame soot temperature and volume fraction distributions demonstrated that the proposed hyperspectral video imaging technique improves the soot temperature and volume fraction reconstruction accuracy.

Keywords: Hyperspectral imaging, soot temperature, soot volume fraction, self-absorption, diffusion flames

1. Introduction

Combustion is a complex multidimensional and time-dependent interaction of chemical reactions with different transport processes such as mass, momentum and energy. Soot thermal radiation is one of the most important and complex phenomena involved in sooting flames and it affects the combustion efficiency, heat transfer, and exhaust emissions (NO_x, CO) [1]. Therefore, it is important to understand the soot formation and oxidation mechanisms in-depth to mitigate soot emissions from practical combustion devices. Over the past years, various optical diagnostic techniques have been developed to investigate soot formation. For example, laser-based techniques such as light extinction [2-4], coupled light extinction [5], laser elastic scattering [7-9] and laser-induced incandescence [10-13] play an important role to measure the soot primary particle size, volume fraction and morphology. These laser-based techniques are suitable for studying the soot optical properties and distribution in axisymmetric flames due to their reliable accuracy. However, laser-based techniques are often used for laboratory-scale flame measurement.

Flame emission-based measurement techniques are also used for soot formation determination due to their rapid response, non-intrusive manners, and ease of set-up complexity [14-16]. These techniques are developed based on the fact that soot is a strong absorber and emitter of light in visible and near-infrared spectrums. The soot temperature and volume fraction can be solved based on the line-of-sight radiation intensity by employing inversion analysis procedures. Instead of using complicated laser optical arrangements, a single RGB camera can provide adequate flame image data to retrieve the two-dimensional (2D) distribution of temperature and soot volume fraction [14-17]. Whereas the three-dimensional (3D) distributions can be achieved through multi-camera systems [18,19]. Moreover, the emerging light-field imaging devices have also been studied for the 3D

flame temperature measurement. A single light field camera can capture the 3D spatial information of the flame emission., from which the volumetric temperature distribution could be reconstructed [21-23]. Thus, emission-based techniques have a better application in both axisymmetric and non-axisymmetric flame measurement compared to laser-based techniques.

However, the radiation information achieved from three spectral wavelengths (i.e., R, G and B) limits the measurement accuracy due to the unknown emissivity of the flame. Therefore, multispectral imaging systems are introduced in soot studies for acquiring wider spectral radiation information [24-32]. For instance, De Iuliis et.al [24] determined the soot volume fraction of ethylene diffusion flames with the flame spectrum of 300–800 nm wavelength acquired by a spectrometer. A similar arrangement is also employed by Snelling et al. [25] to determine the soot temperature and volume fraction. Recently, hyperspectral imaging techniques have been used instead of conventional spectrometers for flame parameter measurements [32-39]. Rather than collecting the spectrum at a single point like a spectrometer, these techniques imaged the target area in progressive scans and acquired the radiation intensity from tens to hundreds of continuous wavelengths with high spatial resolution. For example, Amici et al. [36] proposed a hyperspectral technique to investigate the characteristics of wildfires. Liu et al. [37] measured the axisymmetric diffusion flame temperature and emissivity with a scanning hyperspectral camera and established the relationship between the emissivity and wavelengths. The same hyperspectral camera is also utilized by Si et al. [38, 39] to investigate the characteristics of burning coal particles. However, these hyperspectral systems are mainly suitable for fixed or slow-moving objects and provide limited temporal resolution due to the nature of the image scanning mechanism [40, 41], thus unable to acquire a clear and full-frame hyperspectral image sequence of dynamic flames. Therefore, an advanced computational hyperspectral imaging technology (also known as the snapshot hyperspectral imaging technology) is required for solving the lack of temporal resolution.

The computational spectral imaging systems have been developed based on under-sampling and reconstruction strategies [42] such as computed tomography imaging spectrometer (CTIS) [43], coded aperture snapshot spectral imager (CASSI) [44] and Prism-mask multispectral video imaging system (PMVIS) [45, 46]. Unlike the conventional hyperspectral imaging systems, these computational spectral imaging systems can acquire high-resolution hyperspectral information with a single snapshot, and even capture high frame-rate spectral videos [43-47]. However, the reconstruction error spectrum of CTIS and CASSI is unavoidable due to their inherent shortcomings of spectral imaging principles as well as the sparsity assumption for a natural scene [47]. In contrast, PMVIS provides better image quality and spectral accuracy, but employing this hyperspectral system for flame soot investigation is still challenging due to the complexity of flame spectral distribution.

The main challenge for flame sooting investigation by employing the PMVIS is how to solve the accurate soot temperature and volume fraction with the complicated hyperspectral data. The unknown soot temperature and volume fraction are strongly coupled in the line-of-sight radiation transfer equations, thus resulting in a complicated objective function in the combined reconstruction procedure, especially when self-absorption of the flame is considered [48]. Because the resultant line-of-sight emission intensity expression is no longer an Abel integral equation and poses an additional difficulty in data inversion [33]. Consequently, the self-absorption effect is usually neglected in the previous work [24, 26, 28-33]. Although Snelling and Liu et al. [25, 33] investigated that the influence of the attenuation error would be small for an optically thin flame (usually for lab-scale flames), self-absorption should be considered in flames that are not carefully verified as optically thin or industrial sooting flames.

Therefore, it is important to resolve the self-absorption effect for obtaining an accurate distribution of flame soot properties. A few attempts have been made to investigate this issue [25, 32-35]. For instance, the importance of self-absorption for soot emission was studied by Hall and Bonczyk [6] and Snelling et al. [25]. They also proposed their flame radiation intensity correction methods respectively, to study the effect of self-absorption. Freeman et al. [34] also proposed a method to recover the unattenuated line-of-sight emission intensities based on a two-path approach. However, the self-absorption correction strategy has not been studied to validate the soot investigation systematically [33]. Li et al. proposed a self-absorption correction strategy using six wavelengths and the Tikhonov regularized method [32]. Compared with the traditional two-color method, the self-absorption corrected results proposed by Li et al.[32] is more consistent with the simulated soot temperature and volume fraction profiles. However, the lack of experimental verification makes the reliability of this method questionable. Thus, the self-absorption correction strategy remains a significant problem that can be explored for an accurate hyperspectral emission-based measurement.

In this study, an iterative method is proposed based on the PMVIS snapshot hyperspectral imaging technique to reconstruct the soot temperature and volume fraction distribution of ethylene-air diffusion flames. Based on the acquired high-resolution hyperspectral data, a novel self-absorption correction strategy is proposed and integrated with the iterative method. Numerical simulations were carried out to assess the reconstruction accuracy of the proposed method as well as the robustness, also to obtain optimum parameters of the hyperspectral imaging system. Based on the optimum parameters, an optimized PMVIS is proposed and fabricated. The quality of spectrum acquisition of the proposed system was verified through a spectrometer. Experiments were carried out on lab-scale ethylene-air diffusion flames to validate the proposed system. The reconstructed soot temperature and volume fraction obtained from the experiments are presented and discussed.

2. Measurement principle

2.1 Flame Radiative Imaging model

In this study, axisymmetric co-flow diffusion flames are considered due to their high repeatability and stability, which is regarded as an axisymmetric emitting, absorbing but non-scattering medium [30]. A flame radiative imaging model is established where the flame is divided into various layers of voxels according to the flame size and axial resolution, as shown in Figure 1. The flame self-absorption effect is carefully considered in this imaging model. A hyperspectral imaging system is employed to acquire the monochromatic radiative images under different wavelengths between 550-850nm through the flame radiative imaging model.

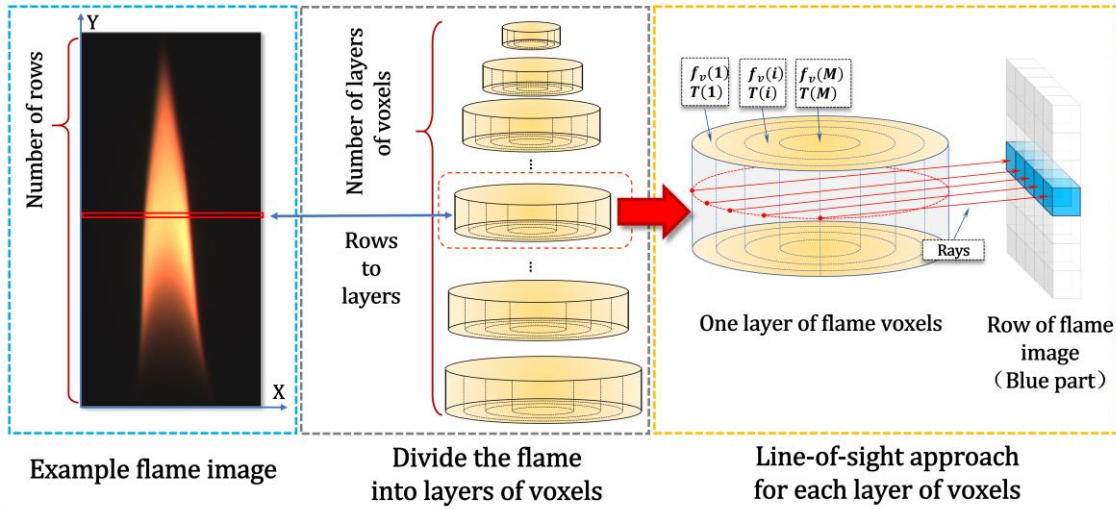


Fig. 1. Schematic diagram of flame imaging model.

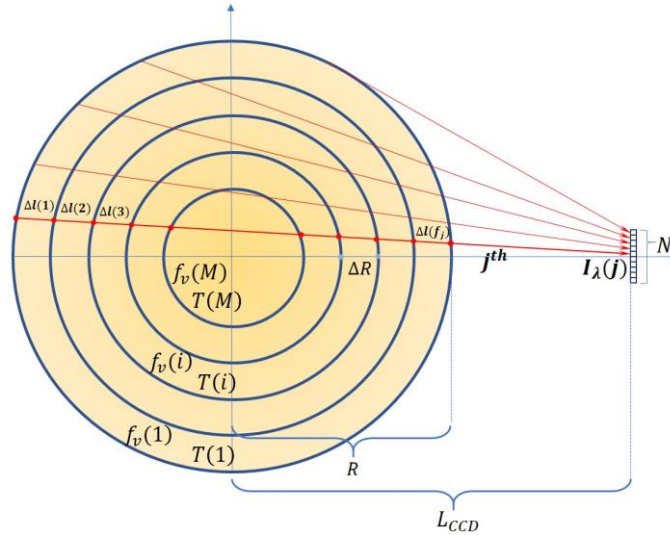


Fig. 2. Example of the line-of-sight imaging model for the flame cross-section, where R is the maximum radius of one layer of flame voxel and each layer contains M concentric cylindrical voxels with equal radius intervals ΔR . In total, N rays are considered that can be recorded by a pixel.

Figure 2 demonstrates the line-of-sight imaging model for a flame cross-section. Flame cross-sectional radiation transmits along the line-of-sight to reach the detector. The Lambert-Beer law [37] is used to obtain the monochromatic radiation intensity $I_\lambda(j)$ along ray j recorded by CCD pixel under the distance L_{CCD} and

expressed by Eq. (1).

$$\begin{aligned}
I_{\lambda}(j) &= \int_{l_0(j)}^{l_f(j)} k_{\lambda}(l) I_{\lambda b}(l) \cdot \exp \left[- \int_{l_0(j)}^{l_f(j)} k_{\lambda}(l') dl' \right] dl \\
&= \int_{l_0(j)}^{l_f(j)} H_{\lambda}(l) \cdot \exp \left[- \int_{l_0(j)}^{l_f(j)} k_{\lambda}(l') dl' \right] dl
\end{aligned} \tag{1}$$

where l refers to the directional path of the radiative intensity recorded by a CCD, thus $\Delta l(i)$ denotes the length of the detection path in the i^{th} voxel. k_{λ} is the local spectral absorption coefficient with a wavelength of λ , which is causally related to the local soot volume fraction f_v . $I_{\lambda b}$ refers to the local monochromatic blackbody radiative intensity with a temperature of T and wavelength of λ . H_{λ} is the local monochromatic emission source term. The attenuation caused by scattering has been neglected as absorption by soot particles is shown to be at least one order of magnitude higher than scattering, especially at large wavelengths in the visible spectrum [24-26].

The local monochromatic blackbody radiative intensity $I_{\lambda b}$ of the i^{th} cylindrical voxel can be obtained as follows [20].

$$I_{\lambda b}(i) = C_1 \lambda^{-5} / [\pi \cdot \exp (C_2 / \lambda T(i))] \tag{2}$$

where $T(i)$ is the temperature of the i^{th} cylindrical voxel. C_1 and C_2 are the first and second radiation constants. In this study, $C_1 = 3.7418 \times 10^{-16} \text{ W} \cdot \text{m}^2$, $C_2 = 1.4388 \times 10^{-2} \text{ m} \cdot \text{K}$.

The Rayleigh–Debye–Gans approximation for polydisperse fractal aggregates (RDG-PFA) has shown good estimates (within 10% uncertainty) of optical cross-sections for soot aggregates, the local spectral extinction coefficient k_{λ_ext} can be related to the soot volume fraction $f_v(i)$ of the i^{th} voxel [49 – 52]:

$$k_{\lambda_ext}(i) = 6\pi E(m) f_v(i) (1 + \rho_{sa}) / \lambda \tag{3}$$

Where ρ_{sa} is the ratio of scattering to absorption and depends on the structure of soot aggregates. The ρ_{sa} can be ignored in most cases when scattering is ignored and k_{λ_ext} is equal to the soot absorption coefficient k_{λ} [24, 51]. Thus, Equation 3 can be expressed as below:

$$k_{\lambda}(i) = k_{\lambda_ext}(i) = 6\pi E(m) f_v(i) / \lambda \tag{4}$$

where $E(m)$ is a function of the refractive index m [53, 54],

$$E(m) = \text{im} | m^2 - 1/m^2 + 1 | \tag{5}$$

Chang and Charalampopoulos expressed $E(m)$ as the following empirical equations [53]:

$$\begin{aligned}
E(m) &= 6nk / (n^2 - k^2 + 2) + 4n^2 k^2 \\
n &= 1.811 + 0.1263 \ln \lambda + 0.027 \ln^2 \lambda + 0.0417 \ln^3 \lambda
\end{aligned} \tag{6}$$

$$k = 0.5821 + 0.1231 \ln \lambda + 0.2309 \ln^2 \lambda + 0.01 \ln^3 \lambda \quad (7)$$

Where n are k real and imaginary parts of the complex refractive index m (i.e. $m = n + ik$). The significance of $E(m)$ is that the accuracy of its value dramatically affects the accuracy of optical diagnostic results. A common approximation of $E(m)$ is 0.26 (while $m=1.57-0.56i$). However, it is too strict to approximate this wavelength-dependent parameter as a fixed value, especially for the multispectral study [54]. Thus, Chang and Charalampopoulos [53] expressed $E(m)$ as a function of wavelength λ , which is employed in this study.

Considering the geometric relationship between the discrete rays and voxels as illustrated in Figure 1, the monochromatic radiation intensity of these rays can be described in the discrete form by Eq. (8).

$$I_\lambda(j) = \sum_{p=1}^{f_j} H_\lambda(j, p) \cdot \Delta l_{j,p} \cdot \exp \left[- \sum_{q=i}^{f_j} k_\lambda(j, q) \cdot \Delta l_{j,q} \right] \quad j = 1, \dots, N \quad (8)$$

Then, Eq. (8) can be written as follows,

$$\mathbf{I}_\lambda = \mathbf{A} \mathbf{H}_\lambda \quad (9)$$

where $\mathbf{I}_\lambda = (I_\lambda(1) \dots I_\lambda(N))^T$ represents the exit line-of-sight radiation intensity (also known as projection intensity) acquired by the imaging system. $\mathbf{H}_\lambda = (H_\lambda(1) \dots H_\lambda(M))^T$ is a local monochromatic emission source. \mathbf{A} is the coefficient factor related to k_λ as well as Δl in each cylindrical voxel.

Assuming that the self-attenuation of the flame is negligible, then Eq. (8) can further be simplified to Eq. (10):

$$I_\lambda(j) = \sum_{p=1}^M H_\lambda(p) \cdot \Delta l_{j,p} \quad j = 1, \dots, N \quad (10)$$

Eq. (10) can be written in matrix form as shown in Eq. (11):

$$\mathbf{I}_\lambda = \mathbf{L} \mathbf{H}_\lambda \quad (11)$$

where \mathbf{L} is the coefficient matrix constituted with the crossing length in each cylindrical voxel of each ray.

2.2 Hyperspectral inversion of soot temperature and volume fraction

The local monochromatic emission source H_λ , representing the radiation intensity emitted by the soot at a wavelength λ , is governed by $I_{\lambda b}$ and k_λ . Thus, considering Eqs. (2) and (4), the soot temperature T and volume fraction f_v can be retrieved directly from H_λ . In this study, the following procedure is employed to determine these two kinds of soot thermal parameters from the H_λ based on the hyperspectral data. According to Eq. (1), for i^{th} voxel, $H_\lambda(i)$ can be expressed as:

$$H_\lambda(i) = k_\lambda(i) \cdot I_{\lambda b}(i) = k_\lambda(i) \cdot (C_1 \lambda^{-5} / \pi \exp(C_2 / \lambda T(i))) \quad (12)$$

Also, it can be written as:

$$\ln(H_\lambda(i) \pi \lambda^5 / C_1) = \ln(k_\lambda(i)) - C_2 / \lambda T(i) \quad (13)$$

where $k_\lambda(i)$ is the local spectral absorption coefficient and it can be expressed as a function of wavelength in the form of the Taylor series expansion:

$$\ln(k_\lambda(i)) = \sum_{j=0}^p a_j \lambda^j (p \leq w - 2) \quad (14)$$

where w is the total number of wavelengths recorded by the hyperspectral imaging system; p is the maximum order of Taylor series expansion for $\ln(k_\lambda(i))$.

Thus, Eq. (13) can be rewritten as:

$$\ln(H_\lambda(i)\pi\lambda^5/C_1) = a_0 + a_1\lambda_i + a_2\lambda_i^2 + \dots + a_p\lambda_i^p - C_2/\lambda T(i) (p \leq w - 2) \quad (15)$$

Eq. (15) can also be expressed as follows:

$$f_i(a_0, a_1, \dots, a_{p+1}) = Y_i - (a_0 + a_1X_{1,i} + \dots + a_pX_{p,i} + a_{p+1}X_{p+1,i}) = 0 \quad (16)$$

where $Y_i = \ln(H_\lambda(i)\pi\lambda^5/C_1)$, $a_{p+1} = -C_2/\lambda T$, $X_{1,i} = \lambda_i$, $X_{2,i} = \lambda_i^2$ \dots $X_{p,i} = \lambda_i^p$, $X_{p+1,i} = 1/\lambda_i$.

Eq. (16) can be expressed more concisely as the matrix form:

$$\mathbf{Y}_{w \times 1} = \mathbf{X}_{w \times (p+2)} \cdot \mathbf{a}_{(p+2) \times 1} \quad (17)$$

The non-negative least-squares (NNLS) method is applied to solve Eq. (17) [23, 55]. Once \mathbf{a} is acquired, temperature $T(i)$ and the local spectral absorption coefficient $k_\lambda(i)$ can be achieved through Eq. (15). Then $f_v(i)$ can be calculated with $k_\lambda(i)$ using Eq. (3).

It is worth noting that the value of p affects the reconstruction convergence and accuracy. Where, the larger the value of p means that the higher-order Taylor series is required to approximate the $\ln(k_\lambda(i))$ and more precise reconstruction can be achieved. However, it is time-consuming. In this study, p is set to 7 [37] by considering a trade-off between reconstruction accuracy and efficiency.

2.3 Reconstruction procedure

Once the emission source \mathbf{H}_λ is acquired with the line-of-sight radiation intensity \mathbf{I}_λ vector (known as projection radiation intensity vector), the unknown soot temperature T and volume fraction f_v can then be estimated. Since flame self-absorption is considered in the proposed imaging model, the unknown absorption coefficient k_λ is integrated to the coefficient factor \mathbf{A} . Thus, it is impossible to solve the Eq. (9) directly to obtain \mathbf{H}_λ . Therefore, an iterative process is proposed to solve the Eq. (9). To estimate an initial emission source \mathbf{H}_λ , self-attenuation of the flame is neglected first, and the Eq. (9) is simplified to Eq. (11). The estimated \mathbf{H}_λ would be updated for an accurate value during the iterative process. Figure 3 describes the iterative process and reconstruction procedure of the proposed method.

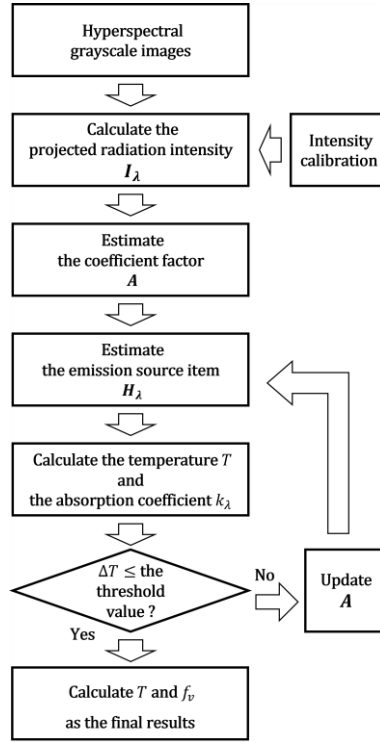


Fig. 3. Reconstruction procedure of temperature and soot volume fraction distribution.

Firstly, estimate the initial value of \mathbf{H}_λ : Self-attenuation of the flame would be ignored first. For one layer of voxels, the coefficient matrix \mathbf{L} can be directly obtained according to the geometric relationship between the light rays and the concentric voxels. Combining the projected radiation intensity vector \mathbf{I}_λ of this layer and \mathbf{L} , the initial value of \mathbf{H}_λ can be obtained using Eqs. (10) and (11) through the NNSL method.

Secondly, to estimate the initial value of \mathbf{A} : The initial temperature value T and absorption coefficient k_λ for each voxel can be achieved by solving Eq. (12). The obtained initial value of the absorption coefficient k_λ is taken into Eq. (9) to estimate an initial result of \mathbf{A} .

Thirdly, to update the \mathbf{H}_λ and \mathbf{A} : \mathbf{H}_λ can be updated by solving Eq. (9) with the initial result of \mathbf{A} and \mathbf{I}_λ . Then, T and k_λ for each voxel is updated again with the latest \mathbf{H}_λ by employing the process described in Section 2.2. Then the coefficient factor \mathbf{A} is updated according to the latest results of the absorption coefficient k_λ . \mathbf{H}_λ and \mathbf{A} are updated until the value of temperature T converged.

Finally, to obtain the final solutions of temperature T and absorption coefficient k_λ . The final solution of soot volume fraction f_v can be acquired with the final k_λ through Eq. (3).

3. Numerical Simulation

3.1 Simulation setup

Numerical simulations were carried out to assess the reconstruction performance and robustness of the proposed reconstruction method. Firstly, simulated flame cross-sections were generated based on the preset soot temperature and volume fraction distribution through the radiative imaging model as described in Section 2.1. It is crucial to consider a reliable preset soot temperature and volume fraction distribution for the numerical simulation for an accurate measurement. Thus, the preset soot temperature and volume fraction distribution are considered based on the flame data proposed by De Iuliis et.al [24], which is experimentally measured and verified. The radiation intensity distribution projected on the simulated CCD is solved under different wavelengths by using Eq. (7). The proposed method as described in section 2 is then used to reconstruct the soot temperature and volume fraction using projected radiation intensity. The parameters of the radiative imaging model are considered in the simulation are summarized in Table 1. The distance between the simulated CCD and the numerical flame center was chosen based on the experiment as described in Section 5. The soot temperature and volume fraction distribution of three different cross-sections (Height above the nozzle = 30, 40 and 50mm) are generated through a cubic spline interpolation algorithm [57] as shown in Figure 4. A comparative study was carried out between the preset and reconstructed temperature and volume fraction distributions to reveal the performance of the proposed method.

Table 1. Parameters of the radiative imaging model

Parameters	Value
Maximum Radius R	4mm
Radius spacing ΔR	0.1mm
Total number of voxels M in one cross-section	40
Total number of rays N in one cross-section	40
Distance between the simulated CCD and flame center L_{CCD}	750mm

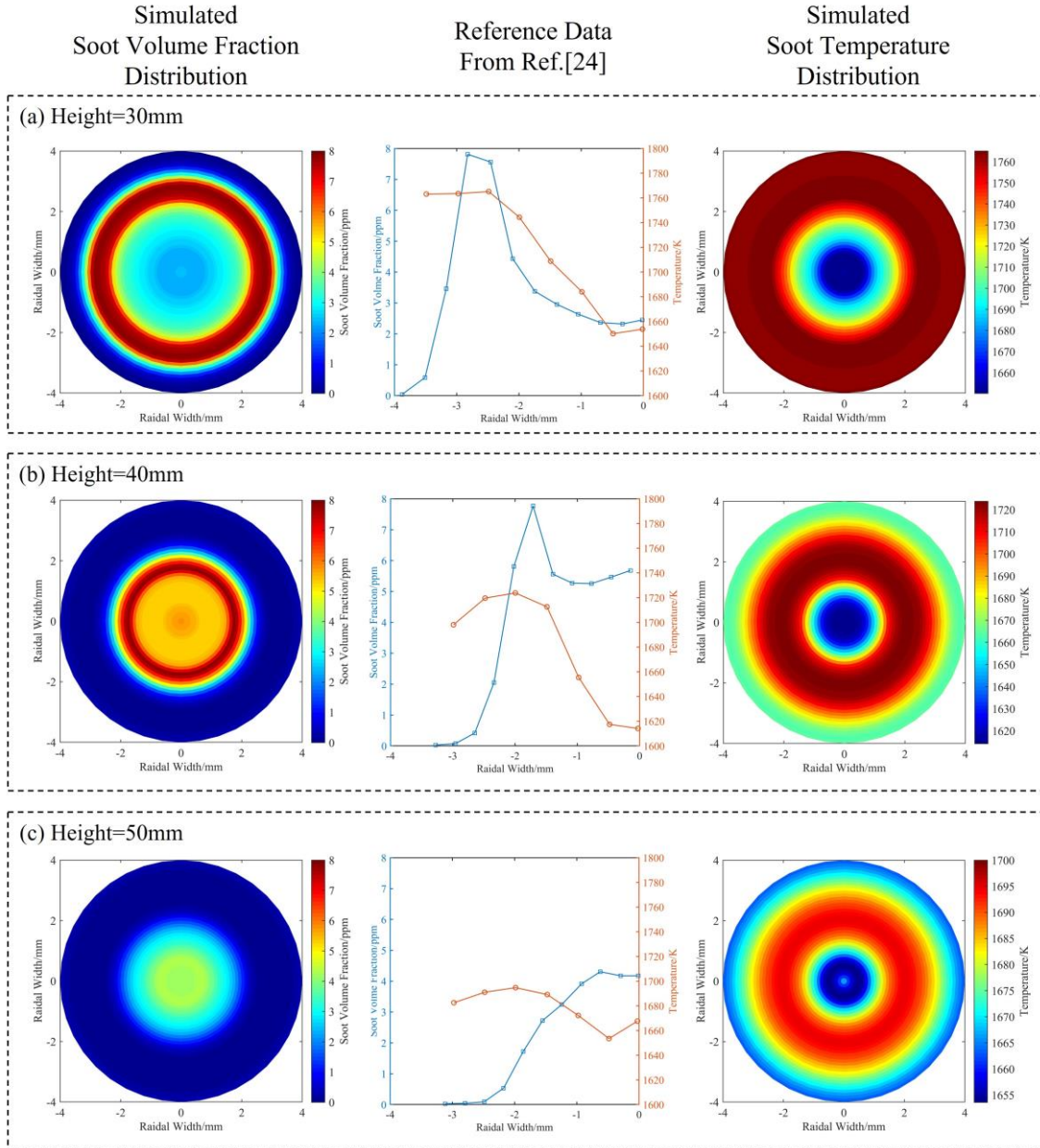


Fig. 4. The simulated axisymmetric flame temperature and soot distribution under three different cross-sections at 30mm, 40mm and 50mm height above the nozzle [24].

3.2 Effects of self-absorption

The effects of self-absorption on the reconstruction accuracy were investigated first. Based on the optical strategy of the hyperspectral system, seven different numbers of wavelength bands are achieved between 550 to 850nm, they are 15, 21, 35, 55, 75, 89 and 128. These wavelength bands are traversed to investigate the effects on the reconstruction accuracy. The case of utilizing 75 wavelength bands was chosen as an example here to explain this investigation procedure. The projection intensity of three simulated flame cross-sections was solved first through the imaging model described in Section 2.1, as shown in Figure 5. The reconstructed temperature and soot distribution were then calculated based on these intensity distributions. Figure 6 presents a comparison between the reconstructed and preset distributions of soot temperature and volume fraction. A similar trend can be seen between the reconstructed and the preset temperature distribution, and so does the

soot. Similar results can also be found for the other cases such as 15, 21, 35, 55, 89 and 128 wavelength bands. Thus, it is evident that the proposed method is self-consistent under five different wavelength bands.

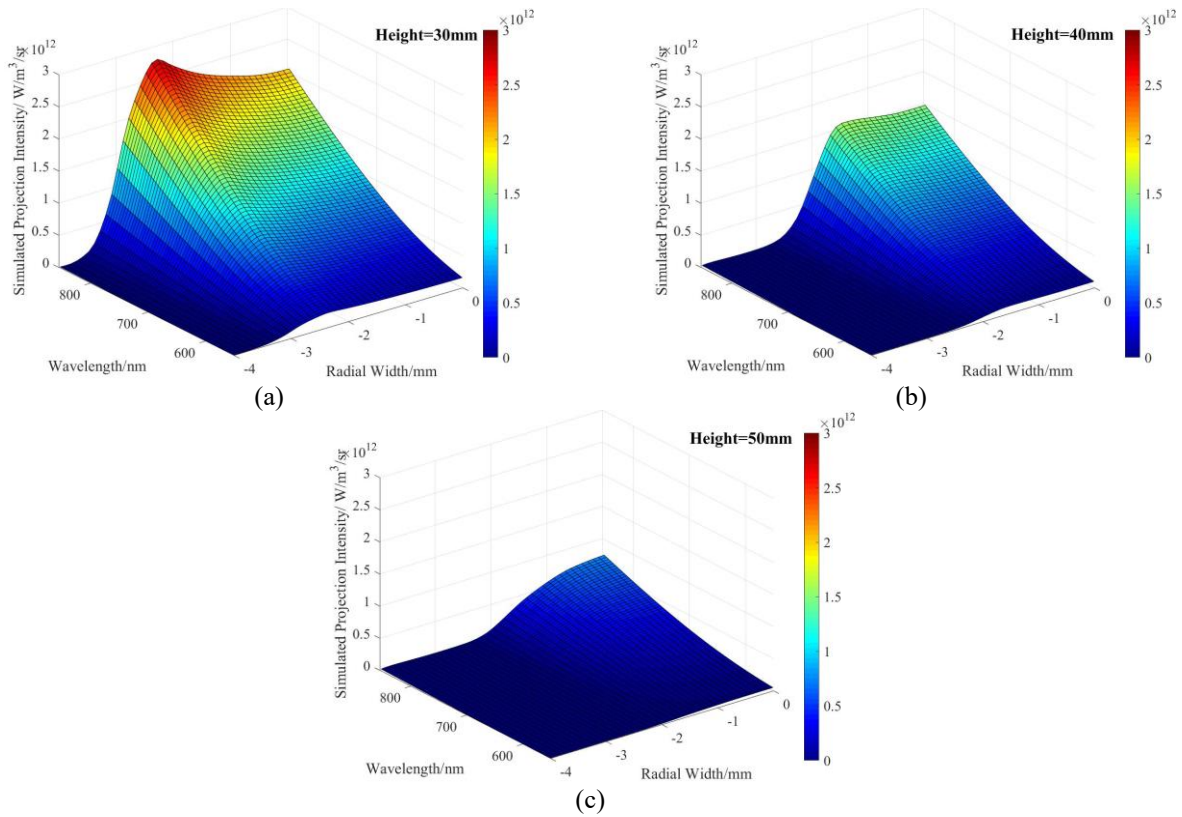


Fig. 5. The simulated projection intensity of the simulated flame cross-sections at (a) 30mm, (b) 40mm and (c) 50mm height above the nozzle.

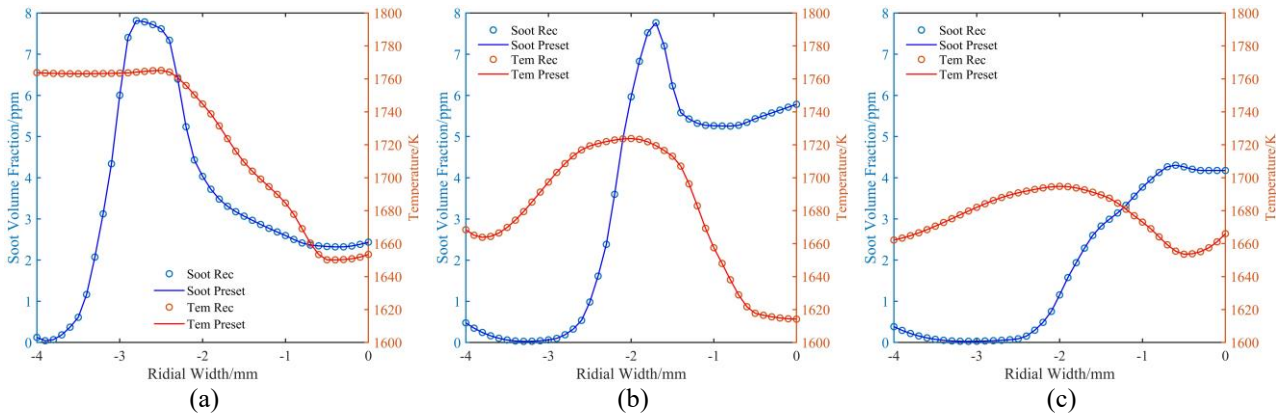


Fig. 6. Comparison between the reconstructed temperature and soot volume fraction (dots) and the preset data (solid lines) at (a) 30mm, (b) 40mm and (c) 50mm height above the nozzle.

Numerical simulations are carried out to study the effect of self-absorption on reconstruction accuracy. In the simulation, a similar setup was adopted as Figure 6. The numerical flame data are derived from Ref. [24], and 75 wavelength bands are used in the reconstruction. The reconstruction results are shown in Figure 7. The reconstructed temperature shows a similar trend as the preset temperature but higher. The reconstructed temperature is 17-25K higher than the preset temperature, with an average of 23.34K. The reconstructed temperatures near the center and the edge of the flame deviate more from the preset temperature. On the other hand, the reconstruction results of the

soot volume fraction are on average 8.22% lower than the preset soot volume fraction. Similar results can also be found in Figures 4b and 4c. For Figure 7b, the reconstruction temperature is 26.51K (average) higher, while the soot volume fraction is 7.42% (average) lower. For Figure 7c, the reconstruction temperature is 20.51K (average) higher, while the soot volume fraction is 9.65% (average) lower. Based on these results, ignoring self-absorption provides a negative effect on reconstruction accuracy. Therefore, the self-absorption correction procedure proposed in this study is necessary to achieve better reconstruction accuracy.

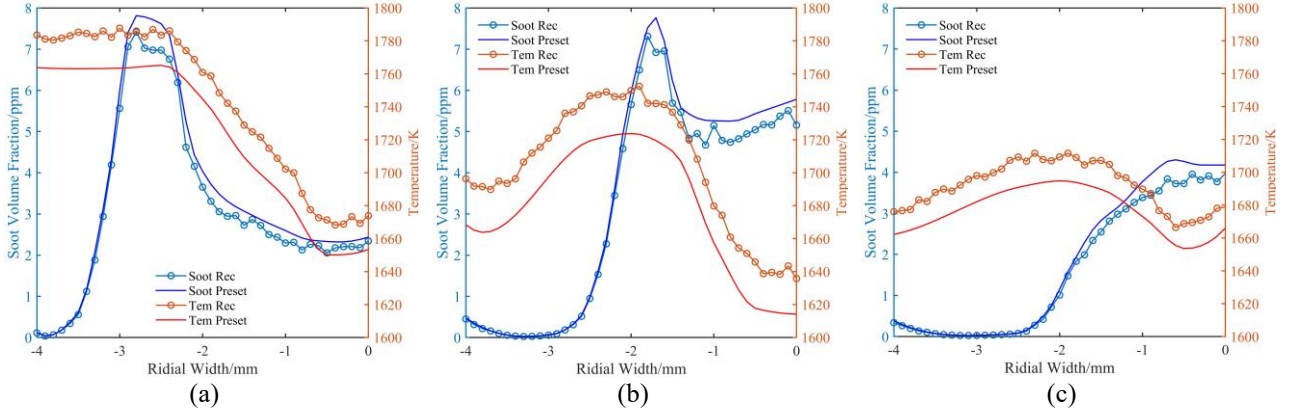


Fig. 7. Comparison between the self-absorption ignoring reconstructed temperature and soot volume fraction (dotted lines) and the preset data (solid lines) at (a) 30mm, (b) 40mm, and (c) 50mm height.

The effect of self-absorption has also been studied by F. Liu et al. [33] and carried out numerical simulations based on Ref. [24]. It has been demonstrated that ignoring self-absorption resulted in an overestimation of flame temperature by 15-31K and an underestimation of the soot concentration by about 10%. This similar conclusion by F. Liu et al. [33] also illustrates the reliability of the proposed results in Figure 7.

3.3 Effects of wavelength bands

The effects of wavelength bands on the reconstruction accuracy were investigated to achieve better integration of the imaging system and the proposed method. In the simulation, no noise is added when examining the influence of the changing wavelength numbers on the reconstruction accuracy. Because the noise-free reconstruction results reflect the difference in the self-consistency of the algorithm accurately. The relative errors of the reconstructed temperature and soot volume fraction are calculated based on the following equations.

$$\delta_{Tem} = 100 \cdot |(T_{Rec} - T_{Preset})/T_{Preset}| (\%) \quad (18)$$

$$\delta_{Soot} = 100 \cdot |(f_{v_Rec} - f_{v_Preset})/f_{v_Preset}| (\%) \quad (19)$$

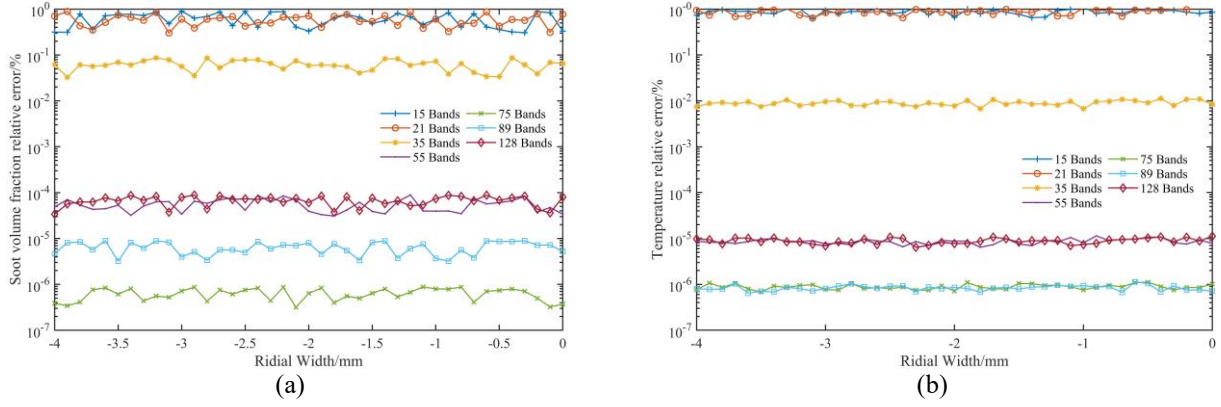


Fig. 8. Relative errors of (a) the reconstructed temperature and (b) soot volume fraction under different cases of wavelength bands at 30mm height above the nozzle.

For example, at height above the nozzle = 30mm the variations of the errors along the axis are insignificant. As illustrated in Figure 8a, δ_{Tem} decreases first when the wavelength numbers increase from 15 to 75. Then, δ_{Tem} under 89 wavelength bands keep a similar distribution with 75 wavelength bands. When 128 wavelength bands are applied the relative errors are the same level as the case of 55 wavelength bands. δ_{Tem} remains lower than 0.0001% when the wavelength bands are more than 35. However, it is hard to distinguish the difference between the δ_{Tem} distribution under 75 and 89, 55 and 128 wavelength bands. Similar situations also occur to δ_{Soot} distribution in Figure 8b. Therefore, it is necessary to take a more concise and intuitive parameter to characterize the reconstruction accuracy under different wavelength bands.

Here, Fréchet distance was utilized to characterize the reconstruction accuracy more concisely and intuitively. Fréchet Distance is a recognized curve similarity evaluation function as expressed by Eq. (18). For instance, let $f: A \rightarrow \mathbb{R}$ and $g: B \rightarrow \mathbb{R}$ be two parameterized curves with homeomorphic parameter spaces of A and B . The Fréchet Distance between f and g can be described as:

$$\delta_F(f, g) = \inf_{\sigma: A \rightarrow B} \sup_{x \in A} \|f(x) - g(\sigma(x))\| \quad (20)$$

where σ ranges only over orientation-preserving homeomorphisms and $\|\cdot\|$ is the Euclidean norm [58]. It can characterize not only the similarity between the point-by-point values on the two sets of data but also between the overall variation trends of these two data sets. Whereas the smaller the value of Fréchet Distance presents the higher the similarity between the two sets of data [58 - 60].

Fig. 9 illustrates the Fréchet Distance between the preset and the reconstructed temperature and soot distribution under five different wavelength bands at 30mm, 40mm and 50mm height above the nozzle. The smaller Fréchet Distance has been obtained when the number of wavelengths bands are greater than 55 and it demonstrates that the reconstructed temperature and soot are highly like the pre-set distribution. This result suggests that the proposed reconstruction method provides a better reconstruction accuracy when the data can be acquired under the 55, 75, 89, 128 wavelength bands between 550nm and 850nm. This also indicates that the hyperspectral imaging system should be designed by using wavelength bands greater than 55 to ensure the reliability of the reconstruction. In practice, these constraints can be considered during the design of the hyperspectral imaging system, which is explained in Section 4.

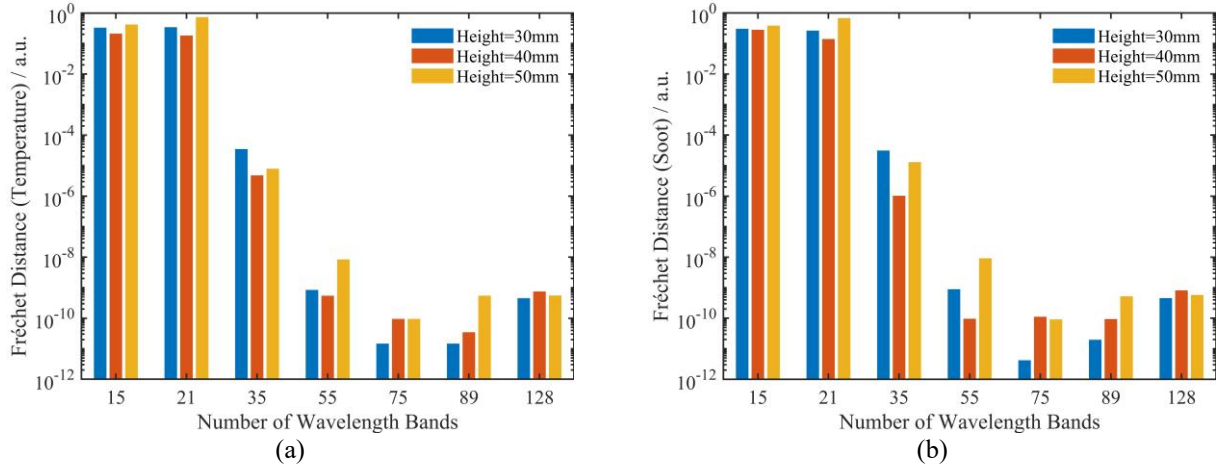


Fig. 9. The Fréchet Distance between the preset (a) soot temperature and (b) soot volume fraction distribution and the reconstructed ones under the different number of wavelengths bands.

3.4 Robustness of the algorithm

It is important to investigate the robustness of the proposed method. Because during the flame acquisition process, inevitable interferences such as noises can be occupied in the radiation intensity. The interferences can also be deposited in the radiation intensity during the digitalization process and thus affects the performance of the reconstruction process. In this study, different signal-to-noise ratios (*SNRs*) are added to the radiation intensity and the *SNR* is defined as follows:

$$SNR = 20 \log_{10}(I_{signal}/I_{noise}) \quad (21)$$

where, I_{signal} and I_{noise} represent the intensity of signal and noise, respectively.

Without noise, the reconstruction accuracy of 55, 75, 89, and 128 wavelengths are better than the 15, 21, and 35 wavelengths. Therefore, the impact of noise at 55, 75, 89, and 128 wavelengths are investigated in this study. The *SNRs* from 60dB to 40dB with an interval of 10dB is added to the simulated flame cross-sections as mentioned in Section 3.1 and are produced at 55, 75, 89, and 128 wavelengths, respectively. The temperature and soot are then reconstructed for these cross-sections and compared with the preset soot temperature and volume fraction distributions. As an example, results achieved at 55 wavelengths are presented here to show the effects of noise. Figure 10 shows a comparison of the reconstructed and preset soot temperature and volume fraction distributions at 55 wavelengths.

The difference between the reconstructed and the preset temperature and volume fraction distributions increases with decreasing the *SNRs*. A significant discrepancy between the reconstructed and the preset temperature and soot can be seen at *SNRs* = 60dB and 50dB, especially at the boundary and center of the flame. However, despite these errors, the reconstructed temperature trends along the radial direction are similar to the preset values. The reconstructed ones accurately represent the peaks, valleys, and fluctuations in the preset temperature and soot volume fraction distributions. Thus, it shows the reconstruction method is reliable at *SNRs* = 60dB and 50dB. In other words, the noise at *SNRs* = 60dB and 50dB are “tolerable” for the reconstruction method.

The reconstruction accuracy is worsened at *SNR* = 40dB. For example, at 30mm, the maximum temperature relative error is 2.62%. It occurs at an axial width equal to -0.7mm, where the reconstructed value is 1694.46k, and the

preset one is 1651.23K, as shown in Figure 2(a3). Although the maximum relative error is less than 3%, when examining the entire reconstructed temperature distribution, it has been noticed that the reconstructed temperature curve fluctuates strangely. These strange fluctuations make the radial trend of the reconstructed temperature distribution very different from the preset value. It is suggested that the SNR = 40dB is not tolerable for the proposed reconstruction procedure. A similar conclusion can also be drawn for the soot volume fraction reconstruction.

Like the description above, analysis of the cases of 75, 89, and 128 wavelengths also obtained their lowest tolerable SNRs. The results are summarized in Table 1 as an essential reference for further hardware optimization. It is suggested that the hyperspectral imaging system with a lower number of wavelength bands should be designed by considering a higher SNR. In this study, the proposed hyperspectral imaging system is fabricated with 55 wavelength bands, which can accurately reconstruct the flame temperature and soot with SNR => 50dB.

Table 2. Relationship between the lowest tolerable *SNRs* and the number of wavelength bands

Number of wavelength bands	SNR (dB)
55	50
75	50
89	50
128	40

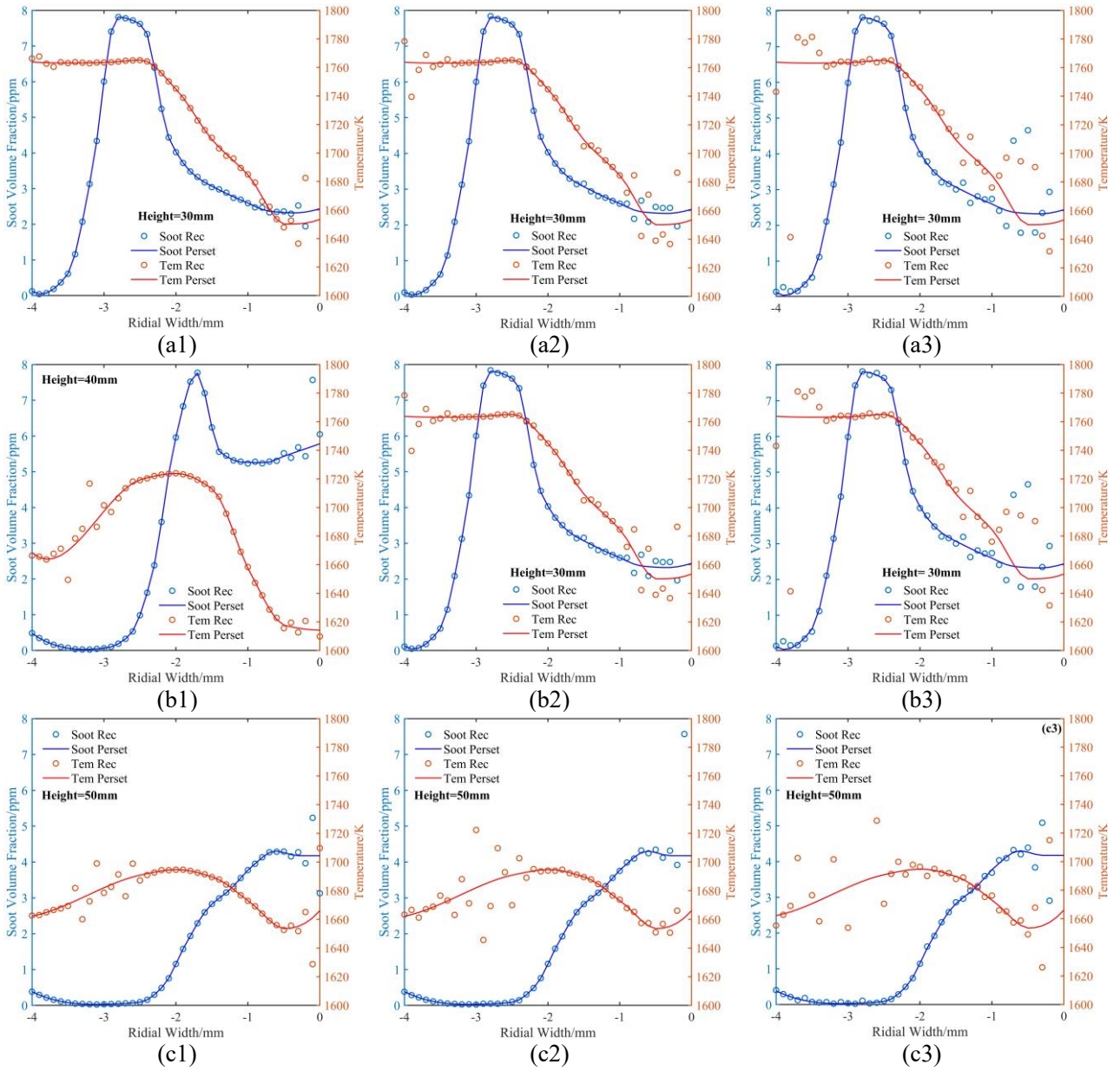


Fig. 10. Comparison between the reconstructed and preset soot temperature and volume fraction distribution at 55 wavelength bands with different SNRs: (a1) (b1) and (c1) at 60 dB; (a2) (b2) and (c2) at 50dB; (a3) (b3) and (c3) at 40dB.

4. Hyperspectral imaging system

4.1 Principle of the imaging system

A hyperspectral imaging system is proposed and fabricated in this study which is mainly based on the concept of Prism-mask multispectral video imaging system (PMVIS) [45-47]. Figure 11 (a) and (b) illustrate the technical strategy of the proposed imaging system. The system mainly consists of an occlusion mask, a prism, a grayscale and an RGB video camera.

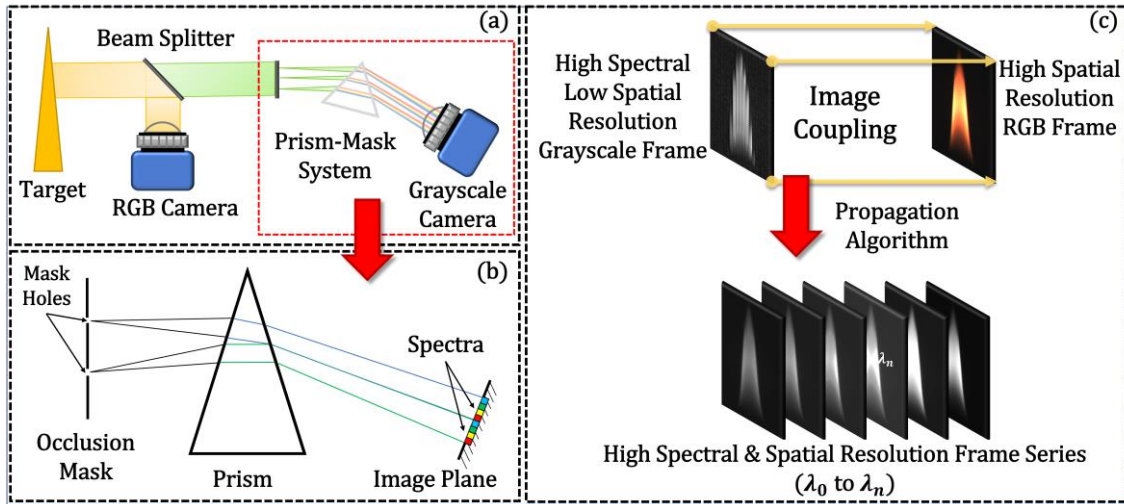


Fig. 11. Overview of the proposed hyperspectral imaging system. (a) schematic of the imaging system; (b) associated components; (c) Overview of hyperspectral video imaging processing.

In general, a hyperspectral data cube with three-dimensional (3-D) spectral data (two spatial and one spectral dimension) can exceed a size of 10 GB. Recording such a large amount of data with a single frame exceeds the limits of Shannon's sampling law [47]. Therefore, in the proposed hyperspectral system, a sparse sample of the target's spectrum distribution is formed by the prism-mask system to ensure that the amount of data for a single frame is within an acceptable range, which can be recorded by a grayscale video camera.

Figure 11(a) and (b) illustrate the hybrid-camera hyperspectral system. For ease of understanding, the devices and optical path are shown as a 2D slice of the actual 3D system. Incoming light from the measured target would reach a beam splitter, which reflects half of the light along the yellow path while transmitting the remainder along the green path. The light on the yellow path is measured in RGB at a high spatial resolution. The light transmitted through the beam splitter (green path) is dispersed by the prism onto the grayscale sensor, which measures numerous channels of its spectra.

As shown in Figure 11(b), the light penetrating through the hole of an occlusion mask can be referred to as the sampling rays. The point on the target that emits these sampling rays are referred to as the sampling points. The number of holes on the occlusion mask determines the possible maximum sampling point of the target within the field of view (FOV). These sampling rays would disperse by the prism into the spectrum and diffuse along with horizontal directions on the CCD sensor so that the intensities at different wavelengths can be recorded by different pixels on the sensor. Thus, the spectral data of this kind of point is directly collected by the system. For each frame of the grayscale, the full-frame image is divided into small regions and each region contains spectral intensity information of the corresponding sampling points.

The triggering of the two cameras is synchronized, such that high-resolution RGB video frames and low-resolution multispectral video frames are captured simultaneously. The two cameras are aligned to capture the same view. Each sampling point of the multispectral imager has a counterpart pixel in the RGB camera that shares the same incoming light ray. The correspondences are used by the propagation algorithm to produce high-resolution multispectral video, just as shown in Figure 11(c) [46]. The system frame rate can be achieved up to 25FPS (frame per second), and is about 175 times faster than that of the commercial hyperspectral camera [37].

The spectral propagation algorithm is mainly based on the color similarity, spatial proximity, and temporal consistency of the low-resolution spectral and RGB video frames. Thus, the number of sampling points for grayscale frames affects the reconstruction accuracy of the algorithm. the greater the number of sampling points, the higher the degree of restoration of the real spectral distribution can be achieved.

4.2 Proposed optimization strategy

The ethylene-air diffusion flame employed in this study has a narrower radial dimension, but its spectral characteristics exhibit obvious variations along with the radial directions. Therefore, the number of sampling points along the radial directions has a significant impact on the reduction of spectral distribution. It is a great challenge to increase the number of sampling points within such a narrow flame.

A simple and reliable approach to increasing the number of sampling points within the flame range is to increase the number of holes on the occlusion mask, where each hole of the mask corresponds to a spectral sampling point. Therefore, the more holes on the mask, the more sampling points can be accommodated within the field of view (FOV) and thus better restoration of the actual spectral distribution can be achieved. However, due to the fixed CCD sensor size, increasing the sampling points means that the number of CCD sensor pixels corresponding to each sampling point would be less as shown in Figure 12. In other words, more sampling points lead to lower available spectral bands for the hyperspectral system.

A trade-off between the number of sampling points and the number of available spectral bands can be considered. Simulation results suggest that (as discussed in Section 3.2), at least 55 wavelength bands are needed to ensure the reconstruction reliability, which is the priority that needs to be met when increasing the sampling points. Based on the lens settings of the proposed hyperspectral system and the experimental burner size, the captured flame image size would not exceed 900(V) x 300(H) pixels. Thus, in this image range, the number of sampling points can be increased from 1250 to 2909 when reducing the number of spectral bands from 128 to 55. But this is still far from satisfactory considering the flame size.

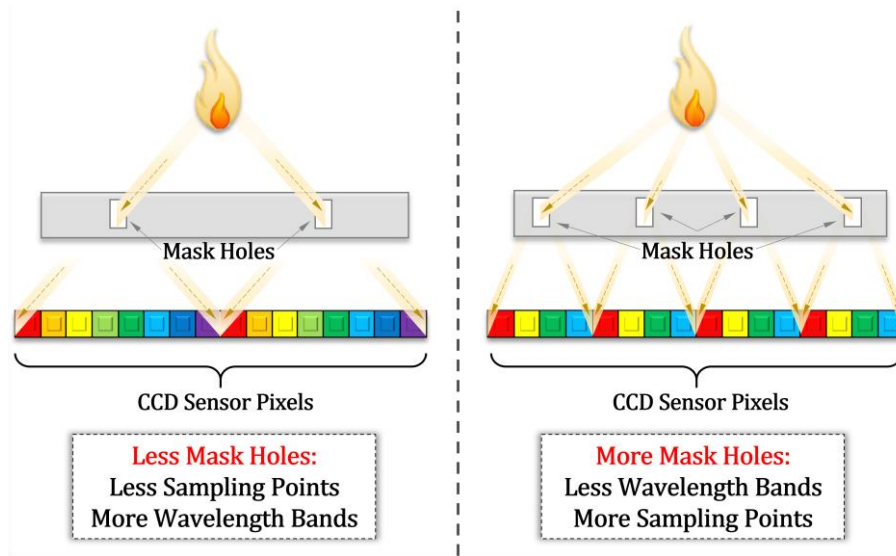


Fig. 12. Influence of changes in the number of mask holes on sampling points and spectral bands.

Further to increase the number of sampling points, two plane mirrors are set up in front of the system to obtain flame images under two additional viewing angles. Figure 13 illustrates the physical construction of the hyperspectral imaging system. The two plane mirrors are set up to reflect the flame images from 30° and -30° angles within the FOV of the proposed system. With the help of these mirrors, three images from 30° , 0° and -30° angles can be recorded by the RGB and monochrome cameras simultaneously. Since the flame is approximately axisymmetric, the images obtained from 30° and -30° angles are highly like the 0° angle, but their corresponding sampling points are different. Therefore, the proposed optical arrangement increases the number of sampling points from 2909 at 0° angle to almost 2909×3 from all three angles, improving the reliability of acquired flame spectral distributions. The spectrum acquisition accuracy of this optimized system is examined and discussed in Section 5.2.

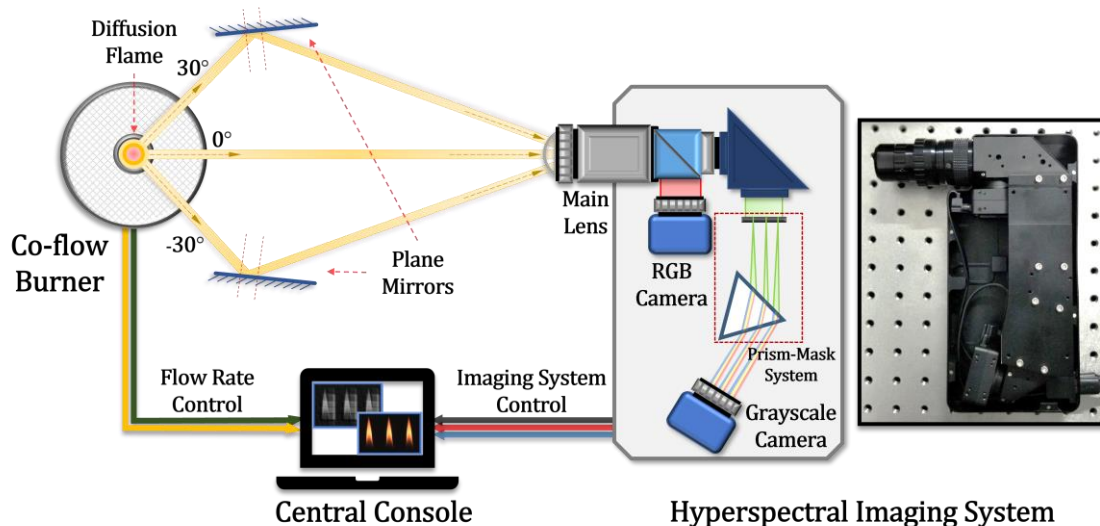


Fig. 13. Schematic diagram of the proposed hyperspectral imaging arrangement.

4.3 Intensity calibration

The hyperspectral imaging system used in this study obtains the electrical signal of the projection radiation of

the flame directly, rather than the radiation intensity value. Therefore, it is necessary to establish a relationship between the grayscale intensity of the CCD sensor and the projection radiation intensity through a blackbody furnace. The blackbody furnace employed in this study is LANDCAL R1500T. The proposed hyperspectral imaging system is used to obtain the grayscale images of the blackbody furnace cavity under different wavelengths and temperatures. The grayscale images of the blackbody furnace are obtained from 1173 K to 1523 K with an interval of 50 K, as shown in Figure 14. During the calibration process, the optical parameter settings of the hyperspectral imaging system are kept consistent with the flame experiments. Figure 15 shows a relationship between the radiation intensity and corresponding grayscale at multiple wavelengths (partial results). The curves in Figure 15 are fitted via a second-order polynomial as below.

$$I = a * G_{\lambda}^2 + b * G_{\lambda} + c \quad (22)$$

Here, I is the radiation intensity of the blackbody furnace and G_{λ} is the normalized grayscale under the case of wavelength λ . G_{λ} is normalized to the range between 0 and 1. a , b and c are fitting coefficients, which are obtained during the fitting process. The values of the fitting coefficients and Goodness of Fit R^2 are listed in Table 2 below.

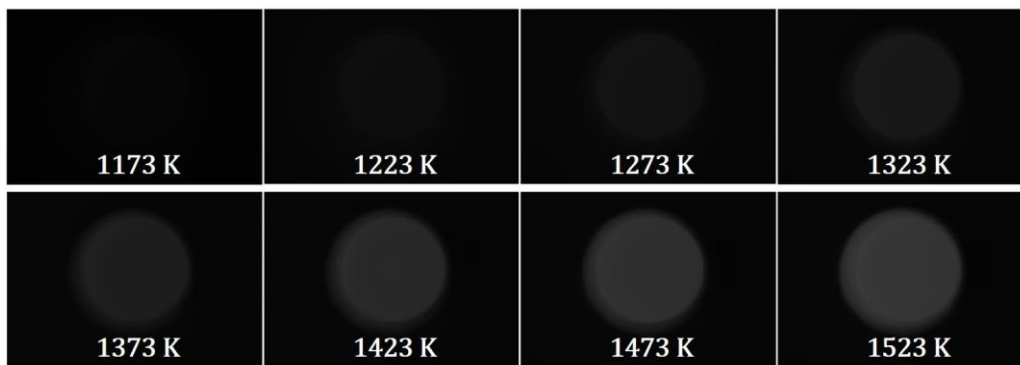


Fig. 14. Example of grayscale images of the blackbody furnace under different temperature settings at wavelength 692.7nm.

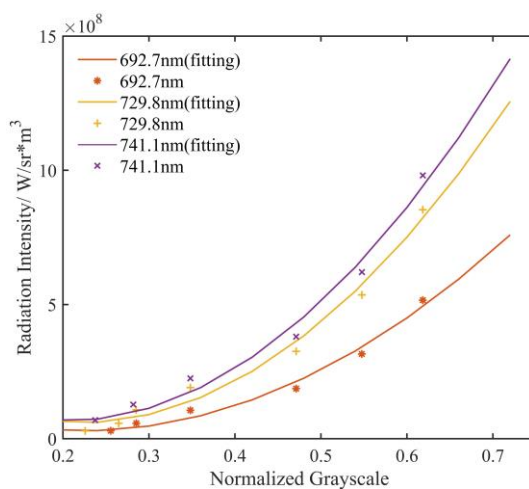


Fig. 15. The relationship between the radiation intensity and corresponding grayscale of the hyperspectral imaging system (partial results).

Table 3. The values of the fitting coefficients and Goodness of Fit R^2

Wavelength	a	b	c	R^2
Case 1: 692.7nm	2.941E9	-1.305E9	1.741E8	0.97506
Case 2: 729.8nm	4.786E9	-2.105E9	2.907E8	0.97683
Case 3: 741.1nm	5.047E9	-2.048E9	2.737E8	0.97709

5. Experimental Results and Discussion

5.1 Operation conditions

To generate a stable flame, a co-flow burner is used in this study. The co-flow burner is consisting of a vertical central brass duct, which has an 11 mm effective diameter of fuel injection [24, 25]. The co-flow air is supplied through the concentric 102 mm inner diameter stainless steel cylinder. The air passes through glass beads and porous metal disks to smooth the flow and prevent flame instabilities. The details can be found elsewhere in Ref. [21-25]. The fuel (ethylene) and airflow were controlled by two digital mass flow meters (i.e., Sevenstar CS200A) with an accuracy of 0.01SLM. During the experiments, the fuel flow is set to 0.22 SLM, and the airflow is set to 5 SLM. An example of ethylene-air diffusion flame images under different wavelengths and directions is shown in Figure 16.

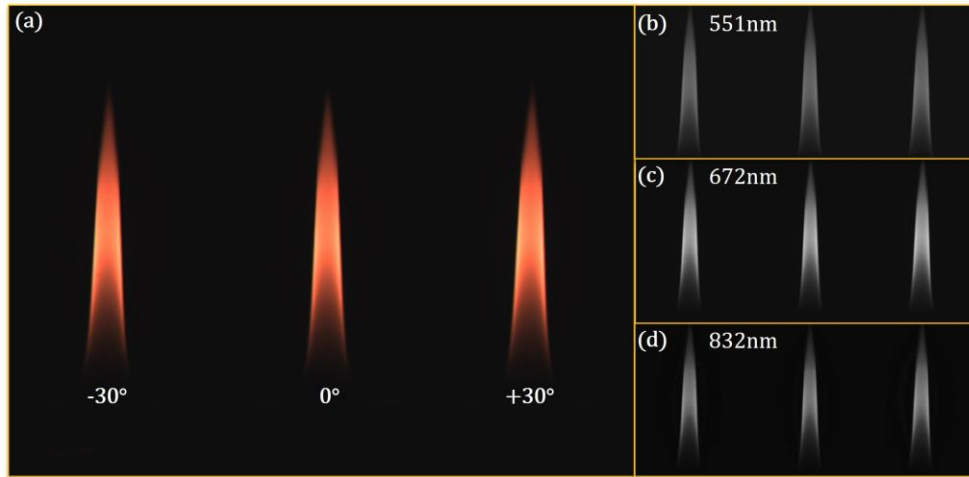


Fig. 16. Example of flame image:(a) Flame RGB images under different directions; (b), (c) and (d) Flame hyperspectral images are extracted at different wavelengths.

5.2 Evaluation of spectrum acquisition

To evaluate the effectiveness of the proposed hyperspectral imaging system, an evaluation of spectrum acquisition was carried out and compared with the existing hyperspectral camera and a spectrometer. The proposed and existing hyperspectral imaging [46] system and a spectrometer (ASD FieldSpec 4) are used to acquire spectral intensity at different heights of an ethylene-air diffusion flame. Note that, the spectrometer only acquired spectral projection intensity at 0° angle which is considered a reference. Figures 17 - 19 illustrate the flame radial spectral intensity acquired by the spectrometer and these hyperspectral imaging systems under

different perspectives. The flame radial spectral intensity obtained by these hyperspectral systems has a similar intensity profile as the reference at 0° angle. The proposed system provides better performance on spectrum acquisition. The flame spectral intensity profiles obtained by the proposed system have a high degree of coincidence with the reference, indicating the effectiveness of the optimization strategy described in Section 4.2.

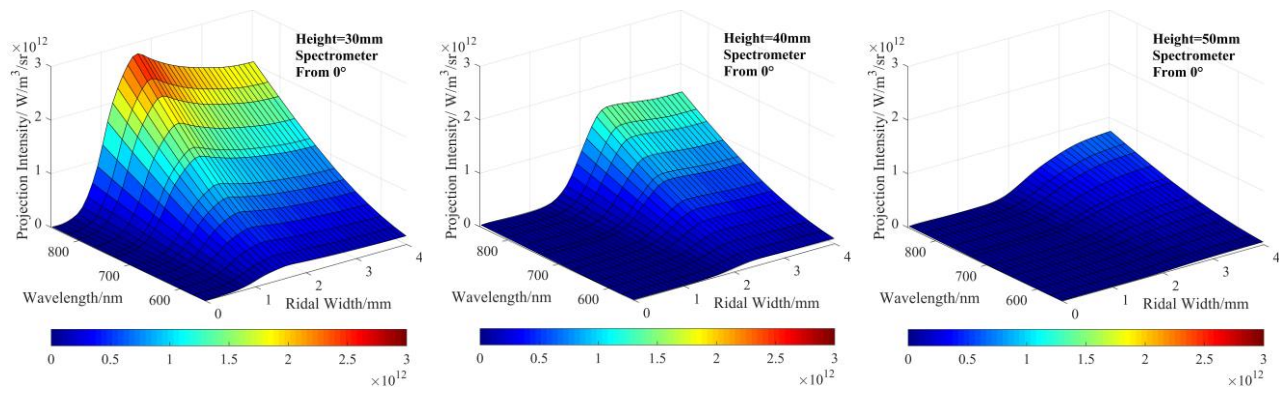


Fig. 17. Flame radial spectral intensity acquired by the spectrometer at three different heights from 0° , which is considered as a reference.

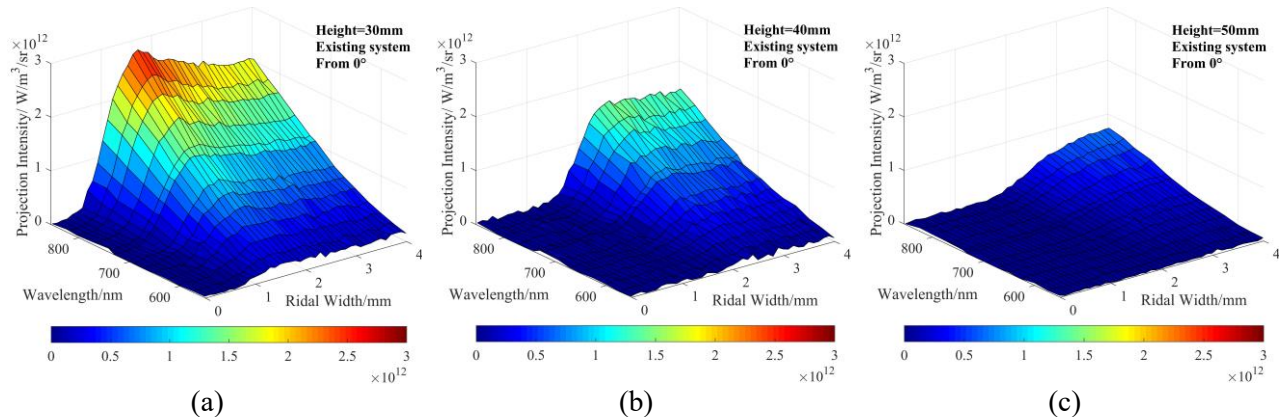
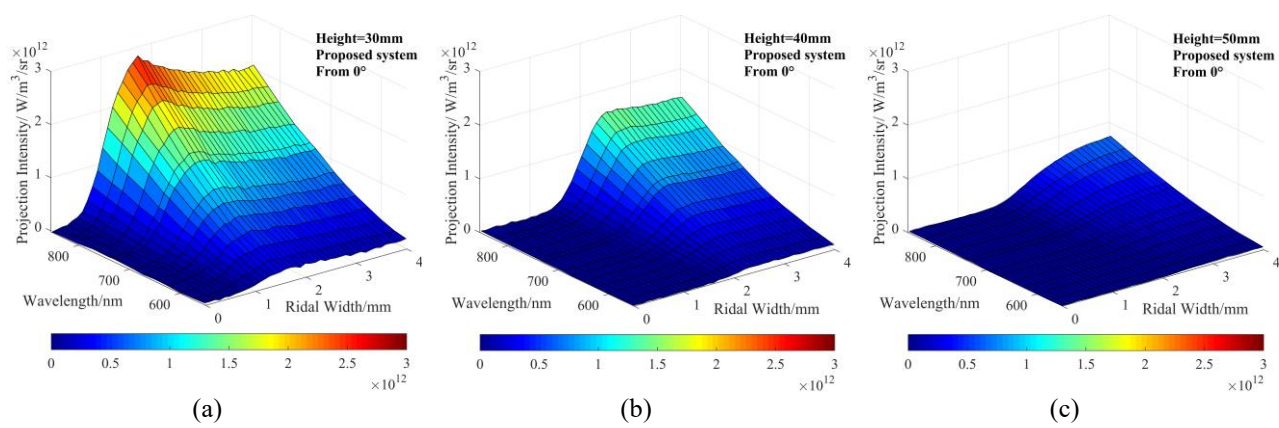


Fig. 18. Flame radial spectral intensity acquired by the existing hyperspectral system at three different heights from 0° .



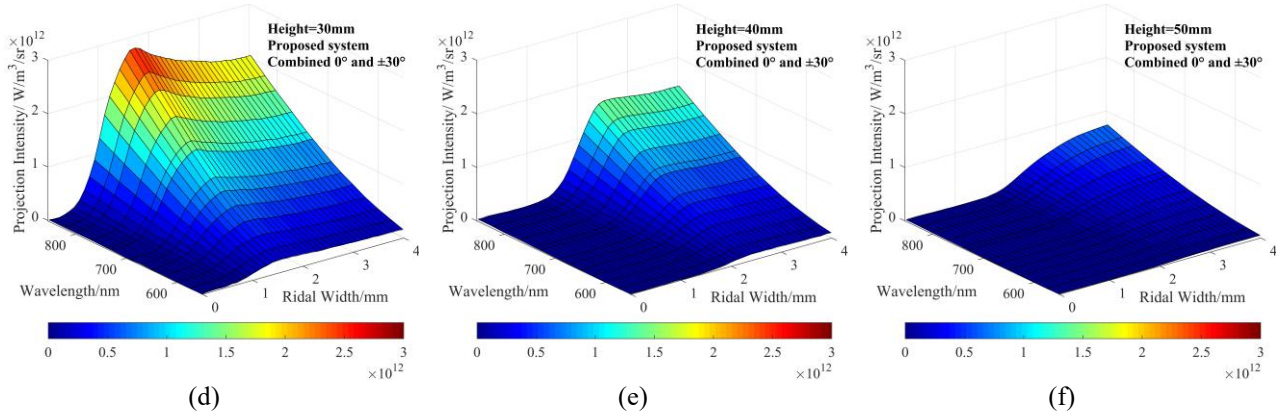


Fig. 19. Flame radial spectral intensity acquired by the proposed hyperspectral system at three different heights. (a)(b)(c) are acquired only from 0° ; (d)(e)(f) are acquired from 0° , 30° and -30° angles.

For an intuitive evaluation of the proposed system, the similarity between the intensity profiles captured by the proposed optimized system and the reference are characterized by Fréchet Distance and shown in Figure 20. The spectral profiles established from the multiple angles are more consistent with the reference acquired by the spectrometer. For example, in Fig. 20(a), the Fréchet Distance of the multiple angles (combination of 0° , 30° and -30°) is 1/3 of the single angle (i.e., 0°). This indicates a better similarity between the spectral profiles established from the multiple perspectives and the reference, showing that the multiple perspectives data improve the accuracy of spectral intensity. A similar conclusion can be drawn for the other two flame cross-sections.

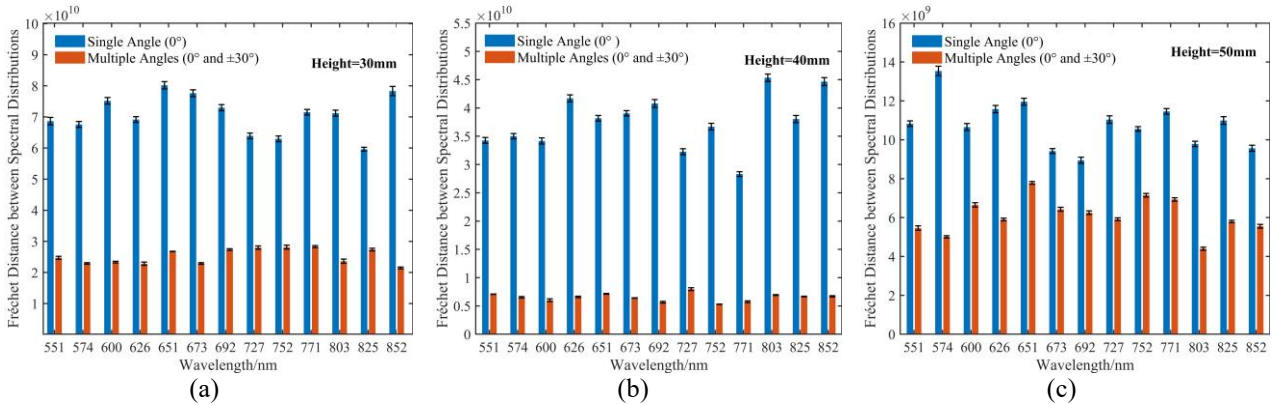


Fig. 20. Similarity (Characterized by Fréchet Distance) between the flame radial spectral distribution acquired by the proposed optimized hyperspectral system at different heights and the reference.

The *SNRs* of the spectral intensity acquired by the hyperspectral system at 0° and multiple angles are calculated using Eq. (21) and shown in Table 3. The measured *SNRs* of radial spectral intensity are all above 50dB under the multiple angles, which means that the measured radial spectral intensities meet the *SNR* requirements of the proposed temperature and soot reconstruction method as discussed in Section 3.4. Therefore, the assessment results demonstrate that the optical optimization strategy considered in this study is useful for measuring spectral intensity accurately and the *SNR* ratio of the proposed hyperspectral system meets the requirements for reliable reconstruction of soot temperature and volume fraction.

Table 3. The measured *SNR* (dB) of spectral intensity at different heights under various angles.

Height above the nozzle	At 0°	Combination of 0°, 30° and -30°
31.1	36.5	56.1
40.4	27.4	55.2
49.7	45.3	57.4

5.3 Reconstruction of soot temperature and volume fraction

To examine the performance of the proposed hyperspectral measurement system, soot temperature and volume fraction of the ethylene-air diffusion flame are reconstructed based on the procedure as described in Section 2. During the experiments, it has been found that the flame is stable but not strictly symmetrical. Thus, the original radiation model in Section 2 was unsuitable for the reconstruction of the experiment flame. To increase the confidence of the results, the flame is treated as a left and right part, i.e., the flame is a combination of two half flames. That is, half of the flame is treated as a collection of semi-annular voxels (elements), and the reconstructions of temperature and soot volume fraction are conducted through this ‘half’ line-of-sight radiation imaging model, as shown in Figure 21. A similar arrangement can also be found in Refs. [25, 33, 37], where the measured flame is also be considered as a combination of two half frames, and the temperature and emissivity (or soot volume fraction) distributions of this half flame are reconstructed through a ‘half’ line-of-sight radiation imaging model similar to this study.

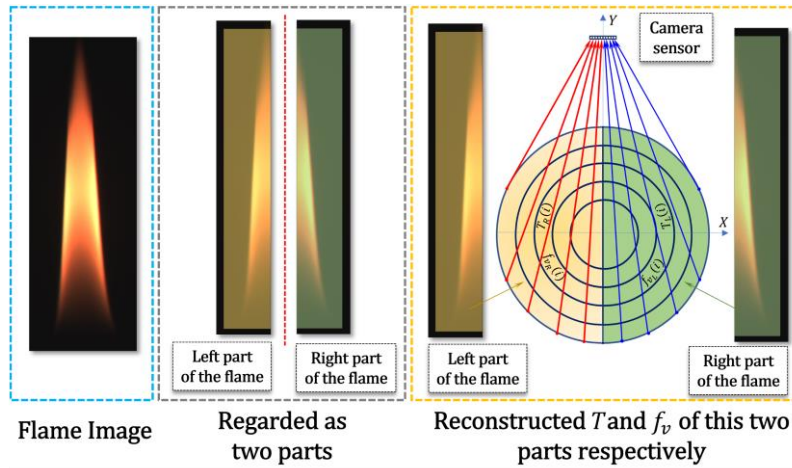


Fig. 21. Schematic diagram of the reconstruction arrangement for the experimentally measured flame.

The soot temperature and volume fraction of these two parts are reconstructed, respectively. Figures 22 and 23 show the reconstructed flame temperature and soot distribution. It can be seen that the measured temperature range is within 1554K to 1971K. The highest temperature zone appears on the flame border at flame heights 30mm to 55mm where the airflow clings to the flame. A lower flame temperature profile can be seen in the middle. A similar profile can be seen for the soot volume fraction. The peak soot volume fraction appears on the outside of the flame near the outside airflow, while the lower soot concentration is in the middle of the flame. Similar soot temperature and volume fraction profiles can also be found in Refs. [21-25, 33, 37, 61]. Results obtained from the experiments ensure the validity of the proposed hyperspectral system for flame soot temperature and volume fraction measurement.

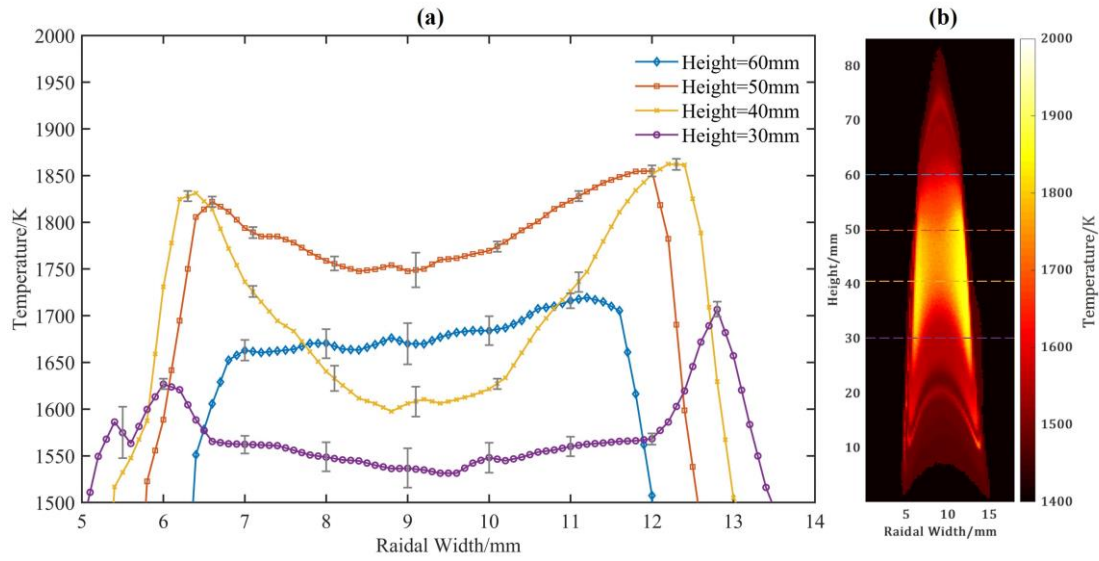


Fig. 22. Reconstructed flame temperature distribution: (a) Cross-section temperature distribution curves of several heights; (b) Soot temperature distribution.

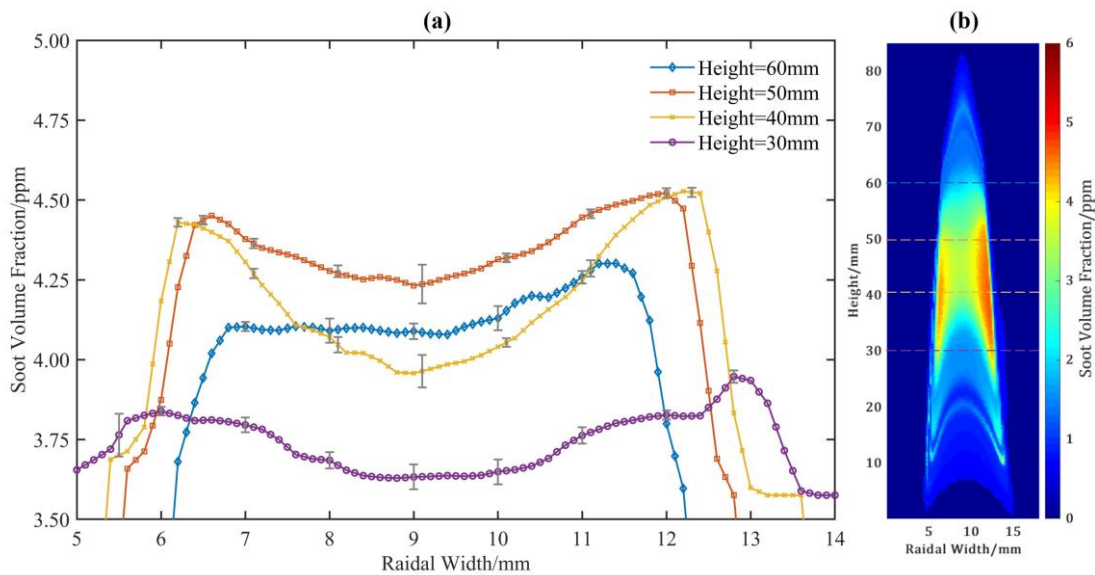


Fig. 23. Reconstructed flame soot distribution: (a) Cross-section soot volume fraction curves of several heights; (b) Soot volume fraction distribution.

It should be noted that some obvious fluctuations of soot temperature and volume fraction can be seen especially at the flame central voxels due to noises in the projection intensity. These noises affect the reconstruction accuracy at the flame center voxels. The flame projection intensity acquired in this experiment is approximately 50-60dB. However, this level of noise is sufficient to cause a visible deviation of reconstruction accuracy, but it does not affect the overall measurement of soot temperature and volume fraction significantly.

To verify the reconstructed results, an R-type high precision thermocouple is used to measure the flame temperature. The flame temperature was measured along the flame diameter at 30mm, 40mm, 50mm, and 60mm above the nozzle.

Figure 10 shows the reconstructed flame temperature compared to the thermocouple measurements. The flame temperature measured by the thermocouple was compensated systematically [60]. At each measurement point, fifty consecutive readings are taken. The standard deviations for these readings are shown as the error bars in Figure 10. The maximum difference between the reconstruction result and the thermocouple result is 67K. It can be noted that the reconstructed radial temperature is similar to the thermocouple measurements, which verified the reconstructed results of the hyperspectral system.

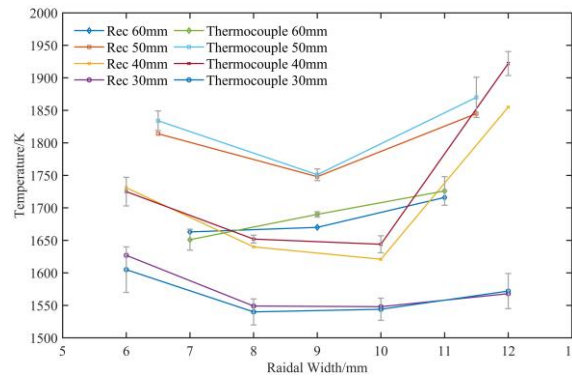


Fig. 10. The comparison of the reconstructed temperatures with the thermocouple measurement.

6. Conclusions

An iterative approach along with a self-absorption correction strategy is proposed to reconstruct the soot temperature and volume fraction of ethylene-air diffusion flames. A hyperspectral imaging system is developed and implemented to acquire flame images under various wavelength bands. It has been found that the self-absorption correction strategy is crucial for an accurate reconstruction of sooting flame temperature and volume fraction. Though neglecting self-absorption correction reduces the difficulty of solving flame radiation, such neglect increases the reconstruction error significantly. The number of wavelength bands of hyperspectral imaging plays an important role to improve reconstruction accuracy. It has been observed that more than 55 wavelength bands (i.e., proposed in this study) provide a better reconstruction accuracy of soot temperature and volume fraction. Also, the larger number of sampling points improves the flame spectrum acquisition accuracy. The proposed hyperspectral system increases the number of sampling points significantly within the field of view, thus improving the signal-to-noise ratio of acquired flame spectrum profiles and providing the target flame is closer to axisymmetric. Experimental results demonstrate that sooting flame temperature and volume fraction can be reconstructed accurately by the proposed hyperspectral system along with the iterative reconstruction procedure, which also indicates the reliability and practicality of the system.

In our ongoing research, the hyperspectral imaging system will be improved further to capture a high-speed video rate so as to meet the requirements of dynamic flame measurements. The imaging model will also be updated to characterize the dynamic flame behavior and to investigate the soot formation mechanism.

Acknowledgements

The authors wish to express their gratitude to the National Natural Science Foundation of China (No. 51976038).

Reference

- [1]. C. Lou, C. Chen, Y.P. Sun, H.C. Zhou, Review of soot measurement in hydrocarbon-air flames. *Science China (Technological Sciences)*, 53 (2010) 2129-2141. <https://doi.org/10.1007/s11431-010-3212-4>
- [2]. W.L. Flower, C.T. Bowman, Soot production in axisymmetric laminar diffusion flames at pressures from one to ten atmospheres, *Proceedings of the Combustion Institute* 21 (1988) 1115–1124. [https://doi.org/10.1016/S0082-0784\(88\)80342-4](https://doi.org/10.1016/S0082-0784(88)80342-4)
- [3]. M.Y. Choi, G.W. Mulholland, A. Hamins, T. Kashiwagi, Comparisons of the soot volume fraction using gravimetric and light extinction technique, *Combustion and Flame* 102 (1995) 161-169. [https://doi.org/10.1016/0010-2180\(94\)00282-W](https://doi.org/10.1016/0010-2180(94)00282-W)
- [4]. J. Zhu, A. Irrera, M.Y. Choi, G.W. Mulholland, J. Suo-Anttila, L. A. Gritzo, Measurement of light extinction constant of JP-8 soot in the visible and near-infrared spectrum. *International Journal of Heat and Mass Transfer* 47 (2004) 3643-3648. <https://doi.org/10.1016/j.ijheatmasstransfer.2004.04.013>
- [5]. A. Khosousi, F. Liu, S. B. Dworkin, N. A. Eaves, M. J. Thomson, X. He, Y. Dai, Y. Gao, F. Liu, S. Shuai, Experimental and numerical study of soot formation in laminar coflow diffusion flames of gasoline/ethanol blends, *Combustion and Flame* 162 (10) (2015), 3925-3933. <https://doi.org/10.1016/j.combustflame.2015.07.029>
- [6]. R.J. Hall, P.A. Bonczyk, Sooting flame thermometry using emission/absorption tomography, *Applied Optics* 29 (31) (1990) 4590–4598. <https://doi.org/10.1364/AO.29.004590>
- [7]. T.T. Charalampopoulos, J.D. Felske, Refractive indices of soot particles deduced from in-situ laser light scattering measurements, *Combustion and Flame* 68 (1987) 283–294. [https://doi.org/10.1016/0010-2180\(87\)90005-8](https://doi.org/10.1016/0010-2180(87)90005-8)
- [8]. C.M. Sorensen, Light scattering by fractal aggregates: a review, *Aerosol Science and Technology* 35 (2001) 648–687. <https://doi.org/10.1080/02786820117868>
- [9]. C.R. Shaddix, K.C. Smyth, Laser-induced incandescence measurements of soot production in steady and flickering methane, propane, and ethylene diffusion flames, *Combustion and Flame* 107 (1996) 418–452. [https://doi.org/10.1016/s0010-2180\(96\)00107-1](https://doi.org/10.1016/s0010-2180(96)00107-1)
- [10]. C. Schulz, B.F. Kock, M. Hoffman, H. Michelsen, S. Will, B. Bougie, R. Suntz, G.J. Smallwood, Laser-induced incandescence: recent trends and current questions, *Applied Physics B* 33 (2006) 333–354. <https://doi.org/10.1007/s00340-006-2260-8>
- [11]. F.S. Liu, B.J. Stagg, D.R. Snelling, G.J. Smallwood, Effects of primary soot particle size distribution on the temperature of soot particles heated by a nanosecond pulsed laser in an atmospheric laminar diffusion flame, *International Journal of Heat and Mass Transfer* 49 (2006) 777-788. <https://doi.org/10.1016/j.ijheatmasstransfer.2005.07.041>
- [12]. F. Patiño, J.J. Cruz, I. Verdugo, J. Morán, J.L. Consalvi, F. Liu, X. Du, A. Fuentes, Soot primary particle sizing in a n-heptane doped methane/air laminar coflow diffusion flame by planar two-color TiRe-LII and TEM image analysis, *Fuel* 266 (2020) 117030. <https://doi.org/10.1016/j.fuel.2020.117030>
- [13]. K.J. Daun, Thermal accommodation coefficients between polyatomic gas molecules and soot in laser-induced incandescence experiments, *International Journal of Heat and Mass Transfer* 52(2009) 5081-5089.

<https://doi.org/10.1016/j.ijheatmasstransfer.2009.05.006>

- [14].W.L. Flower, Soot particle temperatures in axisymmetric laminar ethylene-air diffusion flames at pressures up to 0.7 MPa, *Combustion and Flame* 77 (1989) 279–293. 10.1016/0010-2180(89)90135-1
- [15].T.P. Jenkins, R.K. Hanson, Soot pyrometry using modulated absorption/emission, *Combustion and Flame* 126 (2001) 1669–1679. [https://doi.org/10.1016/S0010-2180\(01\)00278-4](https://doi.org/10.1016/S0010-2180(01)00278-4)
- [16].J. Yon, J. J. Cruz, F. Escudero, J. Morán, F. Liu, A. Fuentes, Revealing soot maturity based on multi-wavelength absorption/emission measurements in laminar axisymmetric coflow ethylene diffusion flames, *Combustion and Flame* 227 (2021) 147-161. <https://doi.org/10.1016/j.combustflame.2020.12.049>
- [17].H.W. Liu; H.C. Zhou, C. Xu, A decomposition method for the simultaneous reconstruction of temperature and soot volume fraction distributions in axisymmetric flames, *Measurement Science and Technology* 31(11) 2020 <https://doi.org/10.1088/1361-6501/ab9dbf>
- [18].M. M. Hossain, L. Gang, D. Sun, Y. Yong, Three-dimensional reconstruction of flame temperature and emissivity distribution using optical tomographic and two-colour pyrometric techniques. *Measurement Science and Technology* 24 (2013) 074010. <https://doi.org/10.1088/0957-0233/24/7/074010>
- [19].M. M. Hossain, G. Lu, Y. Yan, Optical Fiber Imaging Based Tomographic Reconstruction of Burner Flames, *IEEE Transactions on Instrumentation and Measurement* 61 (5) (2012) 1417-1425. <https://doi.org/10.1109/TIM.2012.2186477>
- [20].W. Wien, Die obere Grenze der Wellenlängen, welche in der Wärmestrahlung fester Körper vorkommen können; Folgerungen aus dem zweiten Hauptsatz der Wärmetheorie, *Annalen der Physik*, 285(8) (1893) 633–641. <http://doi.org/10.1002/andp.18932850803>
- [21].J. Sun, M.M. Hossain, C.L. Xu, B. Zhang, S.M. Wang, A novel calibration method of focused light field camera for 3-D reconstruction of flame temperature. *Optics Communications* 390 (2017) 7-15. 10.1016/j.optcom.2016.12.056
- [22].J. Sun, M.M. Hossain, C.L. Xu, B. Zhang, Investigation of flame radiation sampling and temperature measurement through light field camera. *International Journal of Heat and Mass Transfer* 121 (2018) 1281-1296. <https://doi.org/10.1016/j.ijheatmasstransfer.2018.01.083>
- [23].Q. Qi, M.M. Hossain, J.J. Li, B. Zhang, J. Li, C.L. Xu, Approach to reduce light field sampling redundancy for flame temperature reconstruction, *Optics Express* 21 (2021) <https://doi.org/13094-13114>. 10.1364/OE.424112
- [24].S. De Iuliis, M. Barbini, S. Benecchi, F. Cignoli, G. Zizak, Determination of the Soot Volume Fraction in an Ethylene Diffusion Flame by Multiwavelength Analysis of Soot Radiation, *Combustion and Flame* 115 (1998) 253–261. [https://doi.org/10.1016/S0010-2180\(97\)00357-X](https://doi.org/10.1016/S0010-2180(97)00357-X)
- [25].D.R. Snelling, K.A. Thomson, G.J. Smallwood, Ö.L. Gülder, E.J. Weckman, R.A. Fraser, Spectrally Resolved Measurement of Flame Radiation to Determine Soot Temperature and Concentration, *AIAA Journal* 40 (9) (2002) 1789–1795. <https://doi.org/10.2514/2.1855>
- [26].I. Ayranci, R. Vaillon, N. Selçuk, F. André, D. Escudié, Determination of soot temperature, volume fraction and refractive index from flame emission spectrometry, *Journal of Quantitative Spectroscopy and Radiative Transfer* 104 (2007) 266–276. <https://doi.org/10.1016/j.jqsrt.2006.07.013>
- [27].K.A. Thomson, Ö.L. Gülder, E.J. Weckman, R.A. Fraser, G.J. Smallwood, D.R. Snelling, Soot

- concentration and temperature measurements in co-annular, nonpremixed CH₄/air laminar flames at pressures up to 4 MPa, *Combustion and Flame* 140 (2005) 222–232. <https://doi.org/10.1016/j.combustflame.2004.11.012>
- [28].D.S. Bento, K.A. Thomson, Ö.L. Gülder, Soot formation and temperature field structure in laminar propane–air diffusion flames at elevated pressures, *Combustion and Flame* 145 (2006) 765–778. <https://doi.org/10.1016/j.combustflame.2006.01.010>
- [29].H.I. Joo, Ö.L. Gülder, Soot formation and temperature field structure in co-flow laminar methane–air diffusion flames at pressures from 10 to 60 atm, *Proceedings of the Combustion Institute* 32 (2009) 769–775. <https://doi.org/10.1016/j.proci.2008.06.166>
- [30].Ö.L. Gülder, G. Intasopa, H.I. Joo, P.M. Mandatori, D.S. Bento, M.E. Vaillancourt, Unified behaviour of maximum soot yields of methane, ethane and propane laminar diffusion flames at high pressures. *Combustion and Flame* 158 (2011) 2037–2044. <https://doi.org/10.1016/j.combustflame.2011.03.010>
- [31].J. J. Cruz, Luis Fernando Figueira da Silva, F. Escudero, F. Cepeda, J. C. Elicer-Cortés, A. Fuentes, Soot pyrometry by emission measurements at different wavelengths in laminar axisymmetric flames, *Combustion Science and Technology* (2020) Published online DOI: 10.1080/00102202.2020.1825401
- [32].M. Li, Z. He, Research on the effect of soot self-absorption on flame multispectral radiation reconstruction, *Journal of Thermophysics and Heat Transfer* (2020) Published online DOI: 10.2514/1.T5491
- [33].F. Liu, K. A. Thomson, G. J. Smallwood, Soot temperature and volume fraction retrieval from spectrally resolved flame emission measurement in laminar axisymmetric coflow diffusion flames: Effect of self-absorption, *Combustion and Flame* 160(2013) 1693–1705. <https://doi.org/10.1016/j.combustflame.2013.02.007>
- [34].M.P. Freeman, S. Katz, Determination of the Radial Distribution of Brightness in a Cylindrical Luminous Medium with Self-Absorption, *Journal of the Optical Society of America* 50 (8) (1960) 826–830. <https://doi.org/10.1364/JOSA.50.000826>
- [35].F. Escudero, A. Fuentes, J.-L. Consalvi, F. Liu, and R. Demarco, Unified behavior of soot production and radiative heat transfer in ethylene, propane and butane axisymmetric laminar diffusion flames at different oxygen indices. *Fuel* 183 (2016) 668–679. <https://doi.org/10.1016/j.fuel.2016.06.126>
- [36].S. Amici, *New Hyper-Spectral Analysis Methods for Wildfire Investigation and Characterisation*, OECD Summary Report, King's College London, London, UK 2010
- [37].H. Liu, S. Zheng, H. Zhou, C. Qi, Measurement of distributions of temperature and wavelength-dependent emissivity of a laminar diffusion flame using hyper-spectral imaging technique, *Measurement Science and Technology* 27(2) (2016) 025201. <https://doi.org/10.1088/0957-0233/27/2/025201>
- [38].M. Si, Q. Cheng, Q. Zhang, D. Wang, Z. Luo, C. Lou, Study of temperature, apparent spectral emissivity, and soot loading of a single burning coal particle using hyper-spectral imaging technique, *Combustion and Flame* 209 (2019) 267–277. <https://doi.org/10.1016/j.combustflame.2019.08.003>
- [39].M. Si, Q. Cheng, L. Yuan, Z. Luo, W. Yan, H. Zhou, Study on the combustion behavior and soot formation of single coal particle using hyperspectral imaging technique, *Combustion and Flame* 233 (2021) 111568. <https://doi.org/10.1016/j.combustflame.2021.111568>
- [40].D. Manolakis, D. Marden, G. A. Shaw, Hyperspectral image processing for automatic target detection

applications, *Lincoln Laboratory Journal* 14 (1) (2003) 79–116

- [41].A. Bodkin, A. Sheinis, A. Norton, J. Daly, S. Beaven, J. Weinheimer, Snapshot Hyperspectral Imaging—the Hyperpixel Array Camera, *Proceedings of SPIE* 7334 (2009) 73340H. <https://doi.org/10.1117/12.818929>
- [42].D.L. Donoho, Compressed sensing, *IEEE Transactions on Information Theory* 52(4) (2006) 1289-1306. [10.1109/TIT.2006.871582](https://doi.org/10.1109/TIT.2006.871582)
- [43].M. Descour, E. Dereniak, Computed-tomography imaging spectrometer: experimental calibration and reconstruction results, *Applied Optics*, 34(22) (1995) 4817-4826. <https://doi.org/10.1364/AO.34.004817>
- [44].D. Kittle, K. Choi, A. Wagadarikar, D.J. Brady, Multiframe image estimation for coded aperture snapshot spectral imagers, *Applied Optics* 49(36) (2010) 6824-6833. <https://doi.org/10.1364/ao.49.006824>
- [45].X. Cao, H. Du, X. Tong, Q.H. Dai, S. Lin, A Prism-Mask System for Multispectral Video Acquisition, *IEEE Transactions on Pattern Analysis and Machine Intelligence* 33(12) (2011) 2423-2435.
- [46].X. Cao, X. Tong, Q.H. Dai, S. Lin, High resolution multispectral video capture with a hybrid camera system, *IEEE Conference on Computer Vision and Pattern Recognition* 1 (2011) 297-304.
- [47].C. Ma, C. Xun, T. Xin, Q. Dai, S. Lin, Acquisition of High Spatial and Spectral Resolution Video with a Hybrid Camera System, *International Journal of Computer Vision* 110(2) (2014) 141-155. <https://doi.org/10.1007/s11263-013-0690-4>
- [48].Y. P. Sun, C. Lou, H.C. Zhou, Estimating soot volume fraction and temperature in flames using stochastic particle swarm optimization algorithm, *International Journal of Heat and Mass Transfer*, 54(1-3) (2011) 217-224. <https://doi.org/10.1016/j.ijheatmasstransfer.2010.09.049>
- [49].Z.G. Habib, P. Vervisch, On the Refractive Index of Soot at Flame Temperature, *Combustion Science and Technology* 59(4) (1988) 261-274. <https://doi.org/10.1080/00102208808947100>
- [50].S.C. Lee, C.L. Tien, Optical constants of soot in hydrocarbon flames, *Symposium on Combustion*, 18(1) (1981) 1159-1166. [https://doi.org/10.1016/S0082-0784\(81\)80120-8](https://doi.org/10.1016/S0082-0784(81)80120-8)
- [51].A.R. Coderre, K.A. Thomson, D.R. Snelling, M.R. Johnson, Spectrally resolved light absorption properties of cooled soot from a methane flame, *Applied Physics B* 104 (2011) 175-188. <https://doi.org/10.1007/s00340-011-4448-9>
- [52].S.S. Krishnan, K. C. Lin, G. M. Faeth, Optical properties in the visible of overfire soot in large buoyant turbulent diffusion flames, *Journal of Heat Transfer*. 122 (2000) 517-524. <https://doi.org/10.1115/1.1288025>
- [53].H. Chang, T. T. Charalampopoulos, Determination of the wavelength dependence of refractive indices of flame soot, *Proceedings of The Royal Society A-Mathematical Physical and Engineering Sciences* 430(1880) (1990) 577-591. <https://doi.org/10.1098/rspa.1990.0107>
- [54].G.N. Liu, L. Dong, Inverse radiation analysis for simultaneous reconstruction of temperature and volume fraction fields of soot and metal-oxide nanoparticles in a nanofluid fuel sooting flame. *International Journal of Heat and Mass Transfer* 118 (2018) 1080-1089. <https://doi.org/10.1016/j.ijheatmasstransfer.2017.11.084>
- [55].K.C. Smyth, C.R. Shaddix, The elusive history of $m = 1.57 - 0.56i$ for the refractive index of soot. *Combustion and Flame*, 107(3) (1996) 314-320. [https://doi.org/10.1016/S0010-2180\(96\)00170-8](https://doi.org/10.1016/S0010-2180(96)00170-8)
- [56].P.J. Hadwin, T.A. Sipkens, K.A. Thomson, F. Liu, K.J. Daun, Quantifying uncertainty in soot volume

- fraction estimates using Bayesian inference of auto-correlated laser-induced incandescence measurements. *Applied Physics B*, 122(1) (2016) <https://doi.org/10.1007/s00340-015-6287-6>
- [57].T.F. Coleman, Y.Y. Li, An interior trust-region approach for nonlinear minimization subject to bounds. *SIAM Journal on Optimization* 6 (1996) 418–445. <https://doi.org/10.1137/0806023>
- [58].M. Fréchet, Sur quelques points du calcul fonctionnel, *Rendiconti Del Circolo Matematico Di Palermo* 22 (1) (1906) 1–72. <https://doi.org/10.1007/BF03018603>
- [59].Alt. Helmut, M. Godau, Computing the Fréchet Distance between Two Polygonal Curves, *International Journal of Computational Geometry & Applications* 5(1) (1995) 75-91. <https://doi.org/10.1142/S0218195995000064>
- [60].P.K. Agarwal, R.B. Avraham, H. Kaplan, M. Sharir, sampling point, *SIAM Journal on Scientific Computing* 43(2) (2012) 156-167.
- [61].Z.C. Li, L.D. Zhang, C. Lou, In-Situ Measurement of Soot Volume Fraction and Temperature in Axisymmetric Soot-Laden Flames Using TR-GSVD Algorithm. *IEEE transactions on instrumentation and measurement*, 70 (2021) 5001212. <https://doi.org/10.1109/TIM.2020.3010592>
- [62].C.S. McEnally, Ü.Ö. Köylü, L.D. Pfefferle, D.E. Rosner, Soot volume fraction and temperature measurements in laminar nonpremixed flames using thermocouples, *Combustion & Flame*, 109 (1997) 701-720. [https://doi.org/10.1016/s0010-2180\(97\)00054-0](https://doi.org/10.1016/s0010-2180(97)00054-0)